Soil Dynamics and Earthquake Engineering 209 (2026) 110520

Contents lists available at ScienceDirect

Soil Dynamics and Earthquake Engineering

journal homepage: www.elsevier.com/locate/soildyn

An efficient finite element framework for nonlinear seismic soil-foundation-structure interaction in shallow-founded squat masonry structures

Onur Deniz Akan [a,b,*], Massimo Petracca [c], Guido Camata [a], Carlo G. Lai [d], Enrico Spacone [a], Claudio Tamagnini [e]

[a] Department of Engineering and Geology, University of Chieti–Pescara, Pescara, Italy
[b] University School for Advanced Studies IUSS Pavia, Pavia, Italy
[c] ASDEA Software Technology, Pescara, Italy
[d] Department of Civil Engineering and Architecture, University of Pavia, Italy
[e] Department of Civil and Environmental Engineering, University of Perugia, Perugia, Italy

ARTICLE INFO

Keywords:
Nonlinear soil–foundation–structure interaction
Masonry structures
Rocking isolation
OpenSees
IMPL-EX integration
Cracking damage
Ratcheting settlements

ABSTRACT

Fully nonlinear three-dimensional simulations of masonry structures with realistic soil–foundation-structure interaction (SFSI) remain computationally demanding, particularly when capturing material nonlinearity and interface behavior under long-duration seismic excitations. This study presents an OpenSees-based finite element framework that integrates nonlinear masonry, interface, soil-plasticity, coupling, and boundary formulations in a direct SFSI model. The mixed implicit-explicit (IMPL-EX) material-integration strategy is used for the masonry and contact/interface model to improve numerical tractability in large nonlinear dynamic simulations.

The proposed framework is applied to a representative historical masonry tower on fine-grained saturated soil, indicating an interaction mechanism: cracking damage in the foundation masonry results in reduced lateral confinement on the underlying soil. This leads to amplified nonlinear shear distortions, and eventually larger ratcheting settlement accumulation. The response is consistent with rocking isolation observed in reinforced concrete structures, and, in this study, it is studied in the context of historical masonry towers. The results indicate that the rate of soil shear-modulus degradation strongly influences the structural response: steeper degradation limits high-frequency energy transmission, reducing masonry damage at the cost of increased settlement. Comparisons with fixed-base and linear-soil models suggest that neglecting foundation flexibility in the analyzed tower can overestimate seismic demand, whereas neglecting cracking in the foundation masonry can underestimate ratcheting settlement. The residual foundation rotations remain within the adopted serviceability threshold, highlighting a possible trade-off between reduced seismic demand and increased residual foundation deformation. Computational comparisons show that the IMPL-EX formulation reduces solution time relative to fully implicit integration while preserving the relevant global response metrics for the analyzed case.

1. Introduction

Soil–foundation–structure interaction (SFSI) plays a critical role in the seismic response of masonry structures, where the combination of a brittle, anisotropic superstructure and a flexible supporting soil often leads to complex failure mechanisms. The interaction involves nonlinear behavior in both soil and structure, inertial and kinematic coupling effects, site-specific amplification or de-amplification, and nonlinear contact phenomena arising from cracking and pounding between adjacent units, as commonly observed in historical masonry aggregates. In reinforced concrete (RC) frames and bridge piers, previous studies [1], [2], [3] have shown that plastic foundation rotations can reduce superstructure demand and, in some cases, prevent hinge formation. However, the role of nonlinear SFSI in the seismic damage and pounding behavior of unreinforced masonry remains poorly understood.

This study proposes a high-fidelity nonlinear finite element (FE) modeling framework in OpenSees capable of efficiently solving direct dynamic interaction problems and capturing both masonry damage and

* Corresponding author. Department of Engineering and Geology, University of Chieti–Pescara, Pescara, Italy.
E-mail address: onur.akan@iusspavia.it (O.D. Akan).

https://doi.org/10.1016/j.soildyn.2026.110520
Received 3 February 2026; Received in revised form 2 June 2026; Accepted 29 June 2026

foundation settlements. Over the past decades, extensive research has established the foundations of SSI analysis, encompassing soil response theories, kinematic and inertial interaction mechanisms, and numerical methods based on boundary and finite elements [4]. Numerically, SSI behavior is typically modeled through three strategies: substructure, macro-element, and direct approaches. The substructure method decomposes kinematic and inertial components and is suited to linear or equivalent-linear analyses, with soil flexibility represented by frequency-dependent and complex-valued impedance functions [5], [6], [7]. The macro-element method models the foundation-soil system as a single nonlinear element, offering computational efficiency but limited capacity to represent complex interaction phenomena [8], [9], [10], [11]. The direct method treats soil, foundation, and structure as a unified continuum, explicitly accounting for material and geometric nonlinearities as well as boundary dissipation, at the expense of higher computational cost [12].

Time history analysis of nonlinear direct SFSI problems is rare in the literature, mainly due to the prohibitive computational costs of solving large FE models with strong material nonlinearities. Flexible soil–foundation systems have long been recognized as potentially detrimental for relatively rigid or wide masonry structures, where foundation compliance can induce significant differential settlements and increase damage (e.g., ATC, 1996). In contrast [13], observed that foundation flexibility can significantly increase damage in slender towers, while [14] found that neglecting soil deformability through simplified spring models tended to overestimate seismic demand and fragility in rigid masonry structures, with median failure probabilities up to 20–60% higher in some cases. Further evidence of the importance of SFSI in historical towers is provided by the Ghirlandina Tower in Modena, where [15] used ambient-vibration-based identification to show that soil-structure interaction affects the interpretation of the tower dynamic response. For the Carmine bell tower in Naples [16], showed that SFSI can significantly affect the seismic assessment of slender masonry towers, particularly when lateral restraint is absent. They also found that uncoupled or simplified approaches may be non-conservative because they can overestimate structural capacity when soil and foundation failure mechanisms are neglected.

Potential interactions between adjacent historical buildings (such as seismic pounding) are also often ignored, even though they can exchange energy through the soil and amplify damage [17]. [18] investigated linear-structure/nonlinear-soil configurations and concluded that structural vibrations induce larger foundation deformations and settlements [19], [20]. studied the damage response of the bell tower of the Cathedral of Santa Maria Maggiore in Guardiagrele Italy. They assumed linear soil conditions, only P-SV wave propagation, and concluded that linear foundation flexibility induced a demand comparable to the fixed-base case but altered the failure mechanism of the tower. Both used the concrete damage plasticity model available in ABAQUS, which employs a single scalar damage variable. This simplification led to numerical instabilities: large tensile strains caused artificial loss of compressive strength, forcing prior authors to suppress tensile damage or adopt fully plastic behavior [19]. [21] observed that including deformable soil in the seismic model reduced the tower's base-level high-frequency content and modified higher vibration modes [22]. showed that towers with greater slenderness, thinner walls, larger openings, or belfries experienced earlier collapse and larger displacements, suggesting geometry as the dominant factor controlling seismic vulnerability.

Three-dimensional direct modeling has become especially important for shallow-founded structures under seismic loading and potentially liquefiable ground [23]. found strong correlations between intensity measures, such as cumulative absolute velocity (CAV) and pseudo-spectral velocity (PSV), and foundation settlements and rotations [24]. showed that cyclic settlement under local soil liquefaction can result in co-seismic foundation deformations. Foundational work by Refs. [25], [26], [27] extended SFSI analyses to long-span bridges and demonstrated how 3D soil models can improve predictions of out-of-plane seismic effects.

The models for cyclic soil behavior in seismic SSI analysis have powerfully evolved in recent years [28], [29], [30]. Multi-yield surface plasticity formulations, originally introduced by Ref. [31], simulate gradual stiffness degradation through nested yield surfaces in the stress space. Subsequent developments incorporated anisotropic hardening [32], distinct shear moduli for each surface, and combined associative-nonassociative flow rules [33], enabling accurate representation of cyclic hysteresis in sands and clays. These models have been successfully implemented in dynamic SSI [34], [35], [36] and further refined for computational efficiency and strain-softening behavior [37], [38], [39], [40]. Despite these advances in bridge and RC structures, most masonry–soil studies have treated the two materials separately, employing simplified material models either in the soil or in the structure or equivalent springs-dashpots systems rather than direct coupling to nonlinear domains. Consequently, there remains a need for an integrated computational framework that combines advanced damage–plasticity models for masonry with multi-yield plasticity formulations for soil within a unified, dynamically consistent simulation environment capable of resolving contact, uplift, and anisotropy under seismic loading.

A major computational bottleneck arises from the simultaneous treatment of contact nonlinearity within high-fidelity finite element (FE) models. Traditional implicit solvers frequently fail under such conditions, whereas explicit schemes demand prohibitively small time steps to satisfy the Courant–Friedrichs–Lewy (CFL) stability criterion [41]. The implicit–explicit (IMPL-EX) scheme proposed by Ref. [42] and later extended to damage-plasticity by Ref. [43] overcome this trade-off by combining the stability of implicit integration with the efficiency of explicit updates. The internal variables are explicitly extrapolated between steps before performing an implicit stress correction, allowing larger, stable time increments while retaining equilibrium consistency. The resulting algorithmic tangent tensor remains symmetric and semi-positive definite, ensuring convergence even in the presence of material softening. Computationally, IMPL-EX transforms strongly nonlinear problems into a sequence of linearized updates, achieving substantial reductions in solution time without compromising accuracy [42], [43]. This property makes IMPL-EX particularly suited to complex dynamic simulations involving cyclic degradation, frictional contact, and strain softening, provided that time-step control is properly enforced to mitigate extrapolation errors. Recently [44], demonstrated that efficient and accurate dynamic simulations of damage accumulation and seismic pounding is achievable in masonry structures.

This paper presents an efficient finite element framework implemented in OpenSees for the nonlinear seismic analysis of masonry structures with direct soil–foundation–structure interaction (SFSI). The framework integrates material formulations using a mixed implicit–explicit (IMPL-EX) integration strategy that balances numerical stability and computational efficiency, enabling large-scale simulations of cyclic damage, seismic pounding, and soil plasticity. Nonlinearities in both the masonry and soil domains are explicitly modeled, including staged construction and dynamic coupling between foundation rocking and structural response. The approach is demonstrated on the Guardiagrele bell tower, a shallow-founded historical masonry structure, to investigate how soil flexibility influences structural damage, energy transfer, and ground settlement. The proposed modeling framework can be applied to other masonry structures requiring high-fidelity dynamic assessment. Section 2 details the numerical framework and model setup; Section 3 presents the nonlinear seismic analyses. Finally, Section 4 summarizes the main conclusions and implications for future research.

2. Finite element framework for the nonlinear soil–foundation–structure system

This section summarizes the modelling assumptions adopted for the direct nonlinear SFSI analyses implemented in OpenSees [45] and STKO [46]. The model combines a three-dimensional masonry damage-plasticity formulation, a total-stress multi-yield soil plasticity model, embedded-node soil-foundation coupling, viscous/bulky boundary conditions, and parallel solution in OpenSeesMP. The focus is on assumptions that affect the computed seismic response: masonry cracking and stiffness degradation, nonlinear undrained soil response, soil-foundation energy transfer, and computational settings.

Masonry characterization typically relies on flat-jack tests, core extractions, and ambient-vibration measurements, while fine-grained soil characterization requires seismic tests, penetration profiles, laboratory strength/stiffness tests, and index properties. The available data for the present case study [19] were used to define the masonry and soil parameters summarized below.

Surface topography is obtained from digital terrain models (DTMs), which are frequently freely available from municipal datasets, and is incorporated explicitly into the soil-domain geometry. The dimensions of the soil domain are determined by the desired balance between wave-propagation accuracy and computational efficiency. Following the guideline of [19], the soil mass is taken at least 50 times greater than that of the structure to reduce artificial boundary reflections.

The structural model, composed of solid and shell elements, can be generated from architectural drawings or derived from LiDAR point-cloud data. Typically, the masonry structure is modeled at centimeter scale, whereas the surrounding soil extends to the meter scale. To bridge these spatial scales, a transition mesh is introduced between the foundation and soil domains, ensuring smooth stress transfer and compatible mesh density. The design and performance of this transition region are discussed in Section 2.3.

Notwithstanding the use of efficient material algorithms such as the IMPL-EX material integration scheme, the direct SFSI model remains computationally demanding. To address this, a parallel solution strategy is adopted by partitioning the model and executing the analysis in OpenSeesMP. For complex SFSI geometries, a general partitioning procedure tailored to large-scale parallel analysis in OpenSeesMP is presented in Section 2.5.

2.1. Structural masonry model

This section establishes the structural modeling framework forming the superstructure component of the proposed soil–foundation–structure interaction (SFSI) system. The masonry structure is modeled in OpenSees using a three-dimensional anisotropic damage–plasticity formulation that reproduces the cyclic and directional behavior of masonry. The implementation employs the ASDConcrete3D constitutive model [43] combined with the IMPL-EX material-integration algorithm to enhance robustness and computational efficiency in nonlinear dynamic simulations. The IMPL-EX integration provides stable stress updates under cyclic degradation and contact-induced discontinuities while maintaining equilibrium consistency without iterative local return mapping.

Model parameters include the effective elastic moduli, mass density, tensile and compressive strengths, strain at peak compressive strength, fracture energies, and damage–plasticity ratios that define energy dissipation under tension and compression.

The ASDConcrete3D material captures the cyclic degradation typical of masonry, including tension–compression asymmetry, stiffness loss, and residual strain accumulation. Previous studies (17) noted loss of compressive strength following large tensile cycles when a unified damage variable was adopted. To address this, the present formulation employs separate damage variables in tension and compression, improving stability and physical consistency. Numerical stability during cyclic loading and seismic pounding is further ensured by the IMPL-EX scheme, which explicitly extrapolates internal variables followed by a single implicit stress-correction step. This approach improves convergence efficiency compared with fully implicit solvers and is effective in contact-dominated masonry analyses. The key verification and calibration checks used in this study are summarized in Fig. 1, including contact opening-closure, cyclic friction, friction-envelope response, and masonry calibration against cyclic pier tests. Additional implementation details are available in Ref. [44].

The structural domain is discretized with eight-node brick elements for the masonry core and four-node layered shell elements for thin or bending-dominated components such as vaults and floors. Interface coupling between solid and shell elements preserves displacement compatibility and mitigates artificial stress concentrations near contact regions. Fracture-energy regularization is adopted to achieve mesh-objective softening behavior. The resulting formulation is fully compatible with the soil and interface models described in the following sections and forms the superstructure component of the direct nonlinear SFSI framework.

2.2. Soil model for fine grained layers

This section describes the soil domain of the proposed direct SFSI framework, focusing on the dynamic shear response of fine-grained soils under *undrained* loading conditions, while ensuring numerical compatibility with the structural and interface models. The discussion is limited to total-stress analysis, in which volumetric response is blocked by large Poisson's ratio due to full water saturation. Hence, pore-pressure degrees of freedom are not considered here, although the proposed framework is applicable to solid–pressure elements in OpenSees [47] and effective-stress analysis using suitable models such as [29], [30], [34]. Therefore, the computed foundation deformations should be interpreted as co-seismic residual deformations, such as residual foundation rotation at the end of shaking and ratcheting settlement accumulated during cyclic loading, rather than long-term consolidation settlement.

In the proposed framework, accurate transfer of forces and energy across the SSI interface are ensured by consistent soil and structural formulations. Energy dissipation in the structure occurs due to a mix of damage and plastic processes whereas it is modeled through irreversible deformations in soil domain. In OpenSees, the hysteretic loops are described using the PressureIndependMultiYield (PIMY) material [34], [38]. A robust description of the un/reloading response is achieved in small amplitude - high frequency seismic loading due to the memory property of the pressure-independent kinematic hardening formulation. Rayleigh damping of 0.5% at 0.2 Hz and 20 Hz is used to account for low-strain viscous damping in the soil domain.

This framework permits the use of different material-integration schemes within the same finite element model. The soil model is allowed to be implicit when the structure model is IMPL-EX. The PIMY is a relatively simple model without strain softening, and it is computationally efficient. Hence it can be directly used in implicit mode without convergence issues. Using a uniform integration scheme (IMPL-EX in both soil and structure) generally improves numerical stability. An IMPL-EX version of the PIMY model was implemented in Ref. [44], but the computational gain was marginal due to the model's simplicity. Consequently, the mixed IMPL-EX–implicit configuration adopted here provides a suitable balance of efficiency and stability.

Nonlinear soil behavior is governed by the small-strain shear modulus, G_{max}, the undrained shear strength, S_u, and the plasticity index, PI. In the adopted PIMY formulation, S_u controls the limiting undrained shear resistance by defining the size of the ultimate yield surface, whereas G_{max} and the selected modulus-reduction curve control the pre-failure stiffness degradation. These parameters are required by the Vucetic and Dobry stiffness degradation and damping rules [48] for each layer. In Fig. 2a, several well-known degradation rules are compared in terms of normalized shear moduli [48], [50], [51], [52]. The Kondner curve is the default behavior in the PIMY material. However, it results in a nearly elastic–perfectly plastic soil response, which significantly underestimates the relatively low-strain energy dissipation but still overestimates the overall area of the hysteresis loops in real soils

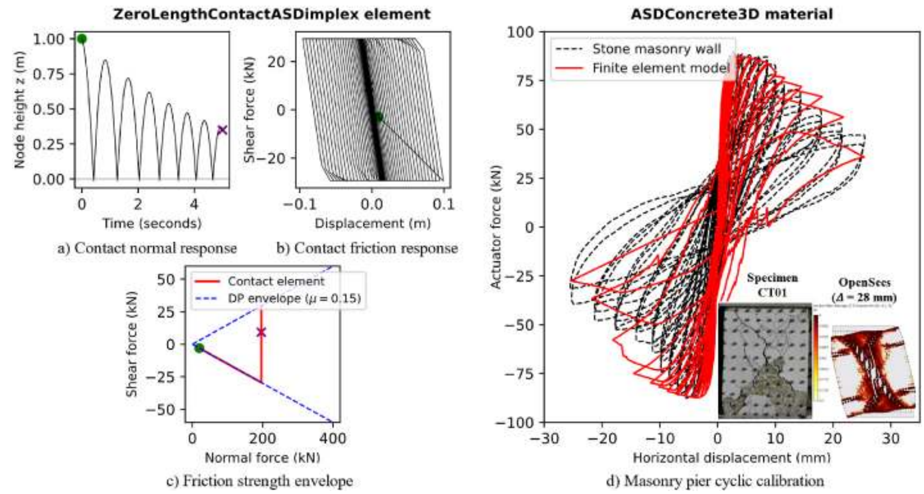

Fig. 1. Verification of interface and masonry formulations: (a) contact normal opening–closure response; (b) cyclic friction response; (c) Drucker-Prager friction strength envelope; (d) ASDConcrete3D calibration against cyclic stone-masonry pier response, including force–displacement behavior and damage localization.

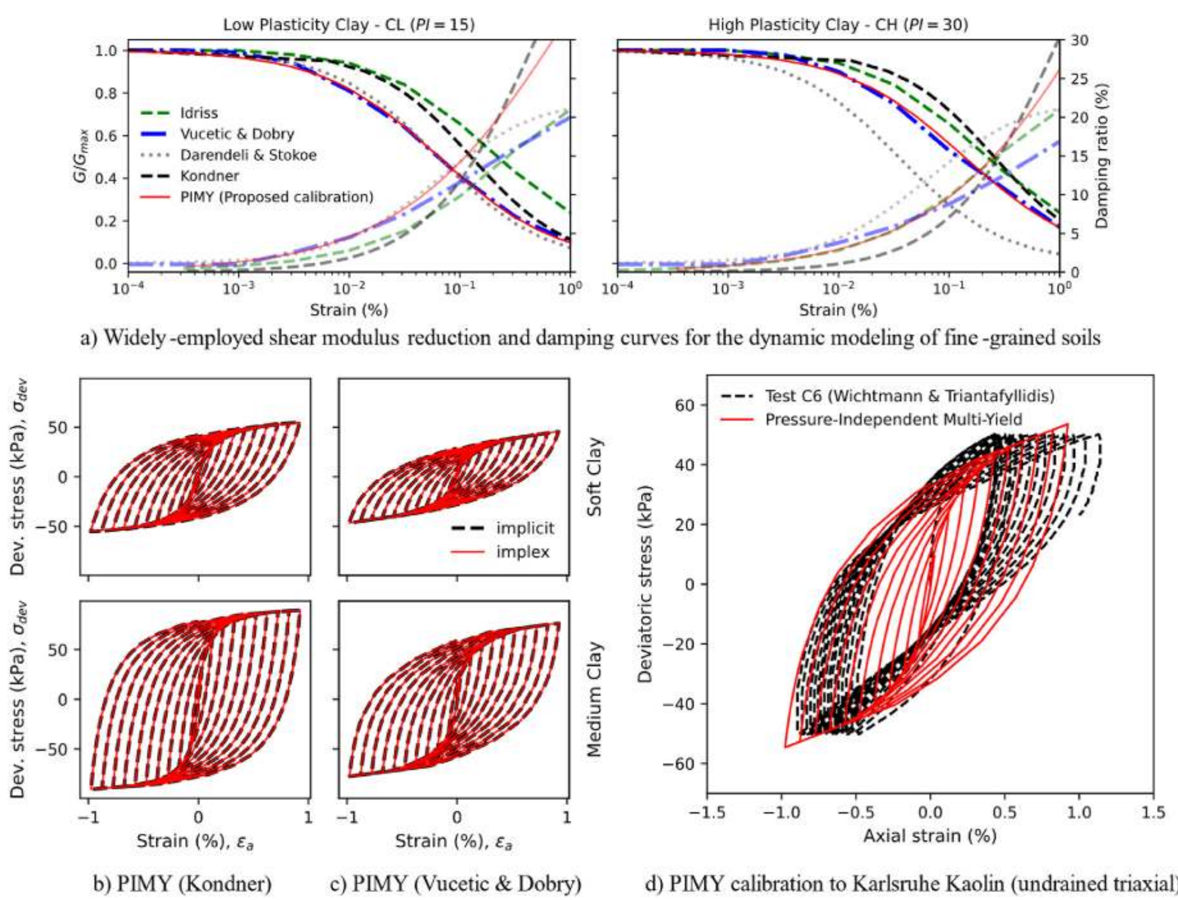

Fig. 2. Calibration and validation of the PressureIndependMultiYield model: (a) comparison of shear modulus reduction curves for clays with different PI, (b–c) cyclic response for soft and medium clays under implicit and IMPL-EX integration, and (d) validation against Karlsruhe Kaolin TX-CU test data [49].

and seismic problems (Fig. 2b and c). In contrast, the Darendeli curve results in larger strains than the Karlsruhe Kaolin [49] specimen data modeled for reference. The Vucetic and Dobry curve is the reasonable mid estimate amongst the considered laws; hence a calibration of the PIMY to match this degradation response is proposed in the framework.

Fig. 2d shows the cyclic response of the adopted PIMY calibration for the Karlsruhe Kaolin specimen [49], together with the corresponding normalized shear-modulus reduction, G/Gmax, and equivalent damping ratio as functions of shear strain. The equivalent damping ratio was computed from the area enclosed by the cyclic stress-strain loops. The PIMY model benefits from a multi-yield surface formulation that provides loading–unloading memory, enabling realistic simulation of frequency-dependent energy dissipation during seismic wave propagation. The current implementation does not permit independent calibration of hysteretic parameters to reproduce target damping–strain relationships. Instead, it relies on modified Masing-type rules, which may overestimate energy dissipation in soft to medium clays such as the Karlsruhe Kaolin (CL class), as evidenced by the excessive loop area in Fig. 2d.

In [48], the PI value is used as a proxy of plasticity in fine-grained material and influenced by factors such as mineral composition, clay particle content, and structure. A high PI value is typically associated with softer, more ductile clays, whereas a low PI indicates higher silt or fine sand content, corresponding to stiffer and more brittle behavior [53].

In the absence of direct testing data, stiffness-to-strength ratios from the literature can be employed, as demonstrated by Ref. [54] and the references therein [53], [54], [55]. proposes estimating undrained shear strength, S_u through G_{max}/S_u or E_u/S_u ratios from the literature for different types of clay, which the former ratio ranging between 150 and 1000. In incompressible analysis, Poisson's ratio should be set to at most 0.49 to prevent numerical issues observed by Ref. [56].

8-node SSP brick elements are used to model the soil domain for efficiency and to prevent potential volumetric locking issues [47]. The element size must accommodate wave propagation with a maximum frequency of 18 Hz in the vertical direction, and it is observed that a minimum of 8–10 elements per minimum wavelength is required to accurately capture wave propagation when considering soil nonlinearity and SSP brick elements. This issue is further discussed in Section 3.2. The topography of the soil domain can be represented explicitly to capture high-frequency (6-12 Hz) surface wave propagation; however, the horizontal spatial discretization must be refined to match the frequency range of interest. In cases where data on sub-surface topography are limited, considering depositional layering or sedimentary processes, the internal structure may be assumed to follow the surface topography. This assumption can result in a 3D soil amplification response equivalent to a 1D model [57]. Finally, the bottom face of the model is truncated as a flat surface by appending a bedrock layer, which simplifies the application of seismic action at the boundaries. The boundary conditions for the proposed framework are discussed in Section 2.4.

2.3. Structure-foundation-soil connection

This section defines the interface coupling strategy forming the third component of the proposed SFSI framework. The goal is to ensure mechanical continuity and energy consistency between the independently meshed structural and geotechnical domains while maintaining computational efficiency. The structural mesh is refined to capture cracking and stress concentrations, whereas the soil mesh is scaled to the shortest wavelengths of seismic waves of interest. The two meshes are connected through a gradual transition zone that enforces displacement compatibility and stress transfer without artificial stiffness amplification.

OpenSees does not include automatic mesh tie or propagation capabilities for solid-to-solid interfaces; therefore, a custom connection framework is developed based on a regularized transition mesh combined with embedded-node coupling (Fig. 3). In this framework, a structured transition box composed of hexahedral elements is used to link the structure foundation and the soil domain. Such an intermediary zone allows for the selective refined meshing of the soil immediately around the foundation which is expected to go under increased plastic deformations due to structure rocking and other kinematic effects. The ASDEmbeddedNode elements are used to tie the domains with different mesh scales. Constraint is provided by attaching the displacements of the constrained node to the displacements of the restraining face of a brick element at interpolation function level. The connection supports both total- and effective stress analyses, enabling consistent modeling across undrained and partially drained analyses.

Compared with a monolithic continuous mesh or a free-form tetrahedral transition mesh, the proposed embedded transition interface drastically reduces element count while preserving smooth stress fields and continuous displacements at the soil–foundation interface. The

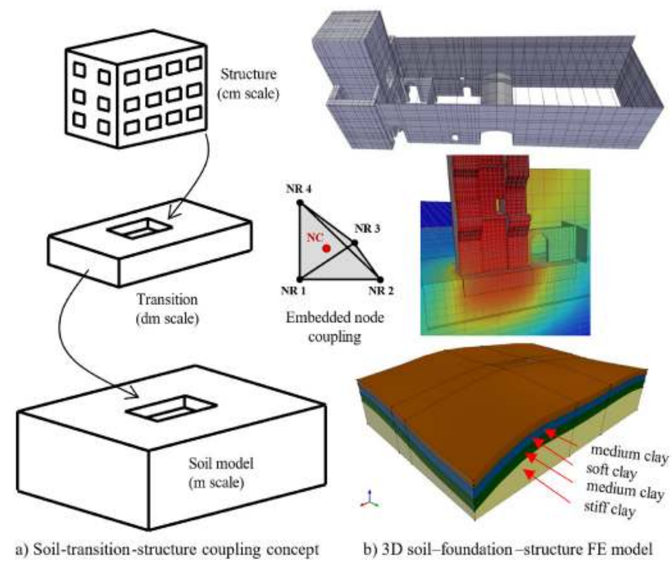

Fig. 3. Soil–structure coupling and FE model configuration: (a) multiscale soil–transition–structure coupling using ASDEmbeddedNode constraints; (b) 3D soil–foundation–structure model showing the tower, transition mesh, soil domain, and modeled soil layers.

element relies on the penalty method to enforce the strength of the connection. The penalty value must provide a stiff enough connection that conserves the continuity of the displacement field. In parallel it should minimize spurious reflections or phase errors that may arise from stiff or over constrained tie elements to provide a physically consistent transfer of seismic energy across the SSI boundary. For wave propagation, this study proposed a penalty term in shear corresponding to an amplification of the medium's shear modulus by a factor ranging between 10^2 and 10^4.

As an alternative, ZeroLengthContactASDimplex coupling can be used to tie two meshes with a discontinuity in between, such as sliding or rocking foundation interfaces or dry joints in pounding interaction [44]. In this case a node-to-node mapping between the interacting meshes is required. The contact elements that take advantage of the IMPL-EX formulation discussed previously in Section 2.1 are available in OpenSees.

It is worth noting that dynamic sensitivity analyses revealed a mesh-size dependency in the foundation settlement response. As the mesh was refined below 1 m, settlement magnitudes increased linearly, whereas for foundation soil elements larger than 1 m, the discrepancy became less pronounced [44]. This dependency arises from the plastic-perfect response of the PIMY material once the critical state (outer yield) surface is activated. Smaller elements accumulate larger strain increments under identical stress paths, reaching this surface earlier and exhibiting exaggerated plastic deformation. This numerical strain amplification is analogous in principle to the inconsistent curvature increment in section response observed in force-based frame elements during the elastic–-plastic transition [58]. Unlike strain localization, this *nonobjectivity* originates from the material formulation, and it can be mitigated through consistent material law regularization or a fully consistent return-mapping algorithm that preserves strain energy equivalence across mesh refinements.

To conclude, other coupling strategies were evaluated to ensure reliable structure–soil interaction [44]. The monolithic mesh approach achieved full nodal continuity but proved computationally prohibitive due to excessive element count and memory demand. The transition zone with a free-form Delaunay mesh reduced the model size but produced discontinuous stress and strain fields at the interface. In contrast, the embedded-node coupling with a structured transition box provided smooth stress transfer and computational efficiency. Therefore, the proposed embedded-node transition method was adopted as the optimal approach, balancing numerical stability, physical consistency, and modeling flexibility.

2.4. Dynamic boundary conditions

In dynamic SSI models, it is essential to distinguish between physical wave reflections, which must be accurately captured, and numerical artifacts introduced by fictitious model boundaries. Physical reflections may arise at material interfaces such as the bedrock–soil contact, at lateral boundaries between geologic units with impedance contrast, or due to topographic irregularities, and they represent an integral part of the seismic response. In contrast, artificial reflections generated at truncated model boundaries can distort both structural and soil responses and must be mitigated through appropriate boundary conditions.

Traditional dissipation strategies available in OpenSees include viscous dashpots (Lysmer–Kuhlemeyer elements) [59], free-field (FF) columns [60], bulky boundary columns [61], and more recently, the domain reduction method (DRM) [62], [63]. Although Perfectly Matched Layers (PML) [64] and the combined LK-FF boundary system [60], implemented in OpenSees as the *ASDboundary* elements provide high transparency for multi-directional wave propagation, their effectiveness diminishes in nonlinear soil models. In both elements, only viscoelastic wave propagation in horizontally layered media is considered by the implementors. While this is effective in elastic regimes, problems arise in nonlinear soil settings due to stiffness mismatches: stiffness degradation in soil cannot be matched by the boundary elements, leading to numerical artifacts or spurious wave emissions from the boundaries. This limitation becomes more pronounced in narrow or deep soil domains.

The DRM approach offers superior performance for absorbing incoming waves and simulating incident seismic motion in nonlinear media [54], [65]. The recent OpenSees implementation [66] allows relatively straightforward application within the proposed framework. However, it requires an additional external viscoelastic domain beyond the model boundaries, which can significantly increase computational cost in large-scale analyses. Moreover, practical considerations such as coupling the internal soil domain with pore-pressure degrees of freedom to the external viscoelastic domain is an open research topic.

As an efficient alternative for cases where near-field structure–foundation interaction dominates the seismic response, a 3D extension of the bulky-column boundary is adopted. This type of boundary is widely-used in 2D liquefaction assessment of wharf structures in OpenSees [61]. In this approach the soil model is terminated with a single layer of enlarged hexahedral elements, approximately ten times wider in the out-of-plane direction. The opposing faces of these boundary elements, aligned with the primary wave propagation direction, are tied using equalDOF constraints to suppress displacement in that direction within the element. The incoming waves are eliminated due to a combination of viscous damping, and the reduced interpolation accuracy inside the bulky elements without the need for extended absorbing layers.

After gravity analysis and stress initialization of the model, all static fixities are released to permit free wave propagation. The gravity-step reactions are then reapplied as equivalent nodal forces to restore equilibrium and prevent spurious transient waves upon fixity release. This procedure ensures three-dimensional wave propagation inside the model and that no artificial stresses are introduced at the start of dynamic analysis. Direct attachment of the boundaries to the soil mesh maintains full kinematic continuity between the model domain and the absorbing layer.

At the model base, LK dashpots are attached to dissipate downward-propagating waves caused by structural motion or reflections from stratigraphy. Dashpot coefficients are assigned consistently with the connected solid-element area. The proposed boundary configuration supports the application of three-component ground motion histories. Input motions are applied as force histories at the model base.

2.5. Computational performance

Parallel computing in civil and earthquake engineering simulations has been extensively explored in prior research [67]. The proposed framework is executed using OpenSeesMP, the MPI-based distributed-memory implementation of OpenSees [68], [69]. The global finite-element mesh is partitioned into subdomains assigned to separate MPI processes. Each subdomain contains a localized subset of elements and nodes, while shared interface nodes are duplicated to preserve inter-partition continuity (Fig. 4).

Nonlinear iterations proceed through parallel local assembly followed by global synchronization and factorization using the MUMPS solver [70]. Solver memory control (ICNTL14) must be calibrated to balance stability and efficiency; for large 3-D SFSI models, a 200–300% workspace over-allocation provides robust performance.

Staged simulation is implemented through a simple initialization sequence. Because OpenSees lacks native element activation or deactivation, all structural and soil elements are initialized at the start to maintain balanced partitions. The structural nodes are initially fixed and decoupled from the soil, forming an independent diagonal block in the global stiffness matrix. Subsequent construction stages release the fixities, activate soil-foundation-structure ties, and apply gravity loads gradually, ensuring consistent parallel solution throughout the workflow.

To substantiate the computational-efficiency claim, Table 1 compares wall-clock solution times for the same SFSI model using implicit, IMPL-EX, and explicit integration strategies under identical hardware and parallelization settings.

Wall-clock times were obtained on a Google Cloud h3-standard-88 instance using identical processor allocation, solver settings, and input-motion duration. The fully implicit analysis lost convergence during the early nonlinear response stage and is therefore reported as a tractability limit, not a full-duration speed comparison. The IMPL-EX formulation completed the simulations at substantially lower computational cost.

3. Application to a historical bell tower structure

The Santa Maria Maggiore bell tower in Guardiagrele, Italy, is a medieval stone masonry structure located on the slopes of the Maiella massif in the central Apennines (Fig. 5). The tower is among the few buildings that survived the Mw 6.8 Maiella earthquake of 1706, which destroyed much of the surrounding town.

The tower reflects typical medieval construction practice, with thick composite masonry walls consisting of dressed stone wythes (1m thick) enclosing a rubble infill (0.8m thick). This configuration yields a heavy, stiff, and a squat structure that is relatively stable under gravity loads but prone to brittle seismic response, governed by coupled flexural and shear mechanisms. In-situ investigations by Refs. [19], [71] including endoscopy and core sampling, suggested high-quality outer stonework and irregular inner composition. The tower geometry was reconstructed from architectural drawings [19] and a 10 $\times$ 10 m Digital Terrain Model (DTM) provided by Ref. [72].

Static loads include self-weight, the 6.4-ton bell system, and dead and live loads on floors. Equivalent masses are assigned to preserve dynamic characteristics, and a rigid diaphragm at the gallery level constrains the adjoining church walls while allowing tower rocking.

The masonry cross-section consists of strong outer stone wythes enclosing weaker rubble infill. Core tests reported compressive strengths up to 6–7 MPa for the outer layer and a stiffness contrast of $\approx$5–6 between outer and inner wythes. Due to limited inelastic data, mechanical parameters (Table 2) were adopted from local seismic codes and refined with experimental studies [73], [74], [75]. Tower-cathedral pounding is

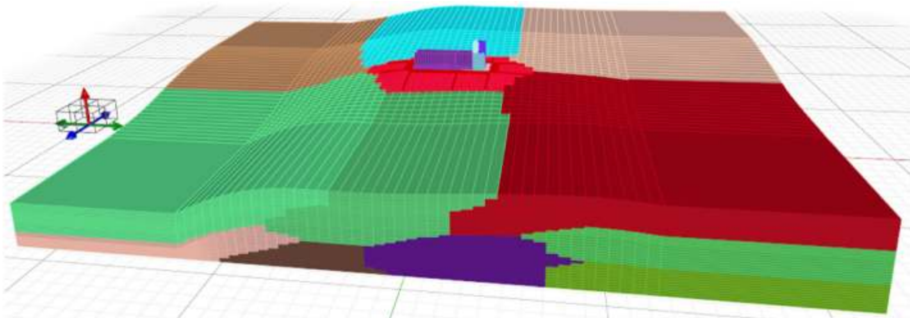

Fig. 4. Parallel domain decomposition of the 3D soil–structure model in STKO [46], illustrating partitioning into 24 MPI subdomains for distributed-memory execution in OpenSeesMP.

Table 1
Computational performance of the nonlinear coupled SFSI analyses under identical hardware and parallelization settings (around 240,000 elements).

Algorithm	Time step (s)	Simulated duration	Wall-clock time	Iterations (avg.)	Relative cost	Settlement (mm)	Outcome
Fully implicit	adaptive (0.005–0.0001)	0.5 s (7%)	108 min	8-10	n.a.	n.a.	Failed (contact convergence loss)
Implicit (IMPL-EX contact)	adaptive (0.005–0.0001)	7.345 s (100%)	75 min	4-5	1.00	−18.0	Completed
IMPL-EX	0.005 (Δt)	7.345 s (100%)	54 min	2 (fixed)	0.72	−18.3	Completed
IMPL-EX	0.0025 (Δt/2)	7.345 s (100%)	90 min	2 (fixed)	1.20	−19.1	Completed
IMPL-EX	0.00125 (Δt/4)	7.345 s (100%)	192 min	2 (fixed)	2.56	−19.6	Completed

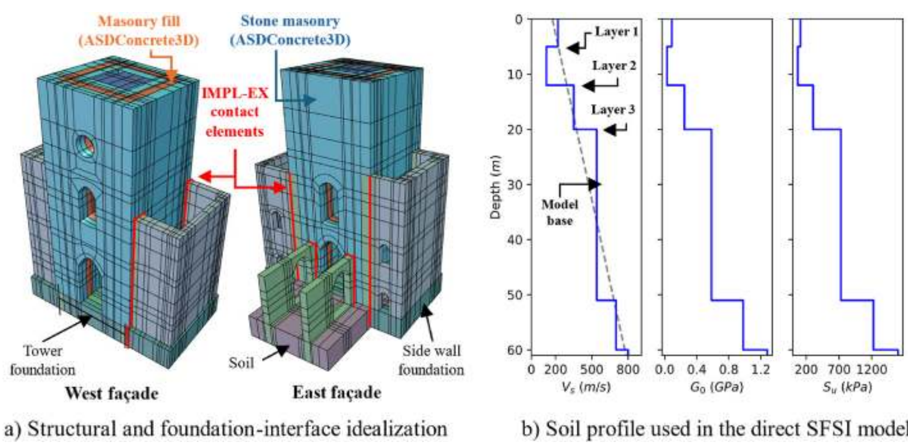

Fig. 5. Main components of the direct SFSI model: (a) masonry material assignment, foundation geometry, soil contact/interface regions, and contact elements with IMPL-EX integration; (b) idealized soil stratigraphy and depth-dependent profiles reported in Ref. [19].

Table 2
Parameters of the ASDConcrete3D material employed for the outer stone masonry, and inner filling (in kN and m).

Parameter	Masonry	Filling	Parameter	Masonry	Filling
rho	2.24	1.94	*fcp*	3300	600
E	3,250,000	700,000	*fcr*	300	100
ν	0.15	0.15	*ep*	0.0025	0.002
ft	120	40	*Gc*	12	4
Gt	0.1	0.05	*PSc_T*	0.40	0.40
fc0	100	400	*PSc_C*	0.50	0.50

modeled using frictional contact elements with a masonry-to-masonry friction coefficient of 0.5.

A refined façade mesh (≈0.5 m) is adopted to capture cracking mechanisms with selective coarsening in less critical regions (Fig. 5b). The out-of-plane behavior is captured through employing elements along the wall cross-section or equivalent fiber section layers in shells.

The calibrated FE model reproduces the measured ambient-vibration frequency bands with good agreement for the dominant translational and torsional modes. This provides an independent check on the global stiffness representation before the nonlinear SFSI simulations.

The subsurface profile was defined from limited borehole data [19], indicating fine-grained, saturated clays. Although no water table was reported, compressional wave velocities (Vp > 1500 m/s) suggest low-permeability, saturated strata. A three-layer configuration was adopted: a fine-grained surface soil (Vs ≈ 220 m/s, PI = 15), a soft clay layer (Vs ≈ 125 m/s, PI = 30), and a medium-stiff basal clay (Vs ≈ 350 m/s, PI = 15). The undrained shear strength, S_u for each layer was derived assuming $G_{max}/S_u \approx 600$ (550 for the over consolidated surface) [53], [54], [55]. Poisson's ratio was fixed at 0.49 to enforce undrained conditions [56]. Shear stiffness degradation was calibrated to empirical G/G_{max} decay as a function of the layer overburden pressure [48], [52]. The model base is located at 30 m depth, where the input motion is applied through the compliant-base boundary

The 3D soil domain captures the hilltop topography of Guardiagrele and ensures a soil-to-structure mass ratio >50, minimizing boundary influence. Vertical element size follows wavelength criteria for accurate propagation up to 18 Hz (minimum 0.7 m in soft soil), and constant 3.6 m horizontal size captures lateral effects up to 4 Hz. The final domain ($\approx 2.25 \times 10^6$ m^3, depth ≈51 m) supports realistic 3D SSI effects including topographic amplification, nonlinear soil response, and rocking–settlement coupling.

To isolate the possible influence of Rayleigh damping, the frequency-dependent viscous damping ratio was evaluated from the adopted Rayleigh coefficients. Although Rayleigh damping was calibrated to 0.5% at 0.2 and 20 Hz, the corresponding damping ratio within the dominant tower response range of approximately 2–4.5 Hz is only about 0.10–0.13%. Thus, the imposed viscous damping provides only minor small-strain dissipation in the frequency range controlling the structural response. The observed high-frequency filtering is therefore attributed primarily to nonlinear soil hysteresis and foundation rocking, rather than to Rayleigh damping.

3.1. Input ground motion

Two representative ground motions were adopted as seismic input for the site of interest. The first is the 1984 Mw 5.9 Lazio-Abruzzo earthquake, previously selected and scaled by Ref. [19] at outcropping bedrock conditions following the NTC 2008 design spectrum [76]. The scaling was performed with reference to the elongated fundamental period of the tower, as estimated from pushover analysis, while spectral compatibility was verified over the period range 0.5 T–1.5 T, in accordance with NTC provisions. This record (Fig. 7a) is used in Sections 3.2-3.4 to enable direct comparison with the results of [19].

The second input set consists of eleven records selected using the conditional spectrum approach based on AvgSA [77] for the 475-year return period at the Guardiagrele bedrock. The record set is selected with the help of EzGM record selection tool [78] and the seismic hazard and disaggregation at the site is calculated using the OpenQuake engine [79] and the European Seismic Hazard Map 2020 source files [80]. The selected suite is shown in Fig. 6, including both the target conditional spectrum and the spectra obtained after nonlinear soil-column propagation. From this suite, the 1984 Mw 5.6 Umbria earthquake recorded at the Gubbio station (SF = 2.7) was selected for the sensitivity analyses in Section 3.4 since its spectral content is representative of the suite over the period range relevant to the tower response.

For the fixed-base analyses, nonlinear (or linear, when applicable) site-response analyses were performed for both records. In the direct SFSI simulations, three-component bedrock seismic motion was applied as vertically propagating waves at the base of the soil domain.

3.2. Nonlinear site response

The nonlinear dynamic response of the Guardiagrele site was analyzed to evaluate soil and topographic amplification. It was also used to verify the adequacy of spatial discretization prior to coupling with the structural model. A series of 1D, 2D, and 3D simulations were performed using the calibrated nonlinear soil model. The 3D response profiles used for comparison with the 1D and 2D analyses are extracted from the central vertical soil column directly beneath the tower foundation, as indicated in Fig. 5b.

First, the reliability of ground amplification modeling was examined through one-dimensional shear column analyses. The linear, equivalent-linear, and nonlinear soil amplification responses are compared to validate parts of the model such as boundary conditions, seismic input, and the soil response (Figs. 7a and 8). The linear and nonlinear analyses were carried out in OpenSees [45] using the proposed approach, whereas the equivalent-linear response was performed using STRATA [81]. The close agreement between the OpenSees nonlinear and STRATA equivalent-linear results indicates the accuracy of the soil model calibration. In the linear model, the site exhibits pronounced amplification near its fundamental period (∼0.4 s). The equivalent-linear and nonlinear analyses both show reduced amplification and a slight period elongation (∼0.45 s), reflecting shear modulus degradation. Shear strain concentrations and Arias intensity in the soft clay (5–12 m depth) indicate the onset of nonlinear response, leading to some energy dissipation in conjunction with ground amplification (Fig. 8).

In Fig. 8, the accelerations at 30 m depth are recorded model responses and not imposed input motions. Difference in base acceleration between 1D versus 2 and 3D models arise from the returning waves that are reflected from topographic features.

Subsequently, a 2D cross section along the east-west direction (global X axis) was analyzed using the same soil layering and material parameters to capture slope effects (Figs. 7b and 9a). In the linear 2D case, topographic focusing enhances acceleration demands at the hill crest, evident in the dashed response spectrum in Fig. 9a. When nonlinearity is introduced, this amplification is partially mitigated by increased hysteretic damping (solid line in Fig. 9a), at the cost of residual displacements developing along the upper slope due to slippage. The residual displacements in layer 2 following a strong cycle of motion are shown in Fig. 7b. Furthermore, a drop in Arias intensity around a depth of 5 m (Fig. 8) indicates that the soft clay acts as a natural isolating layer under strong ground shaking.

Next, the 3D model of the Guardiagrele hilltop is developed to account for multidirectional wave propagation and topographic scattering (Fig. 9b). The analysis includes all three ground motion components

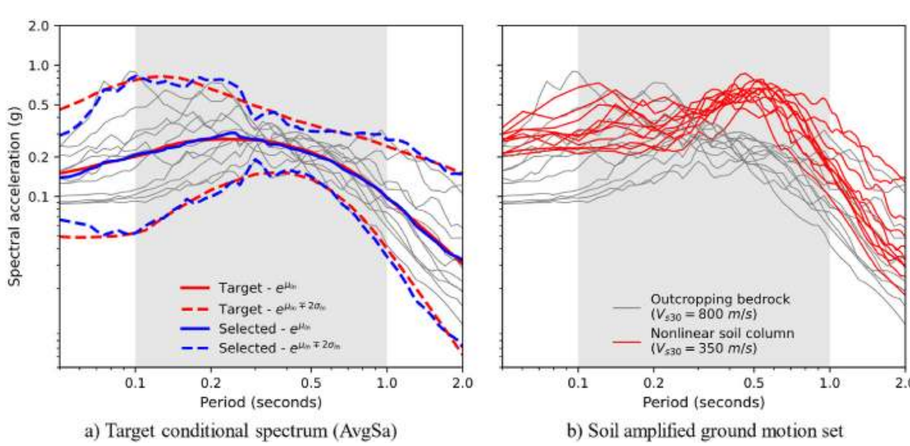

Fig. 6. Selected ground-motion suite: (a) target conditional spectrum and selected bedrock records; and (b) outcropping bedrock spectra and corresponding spectra after nonlinear soil-column propagation. The shaded band indicates the AvgSa period range.

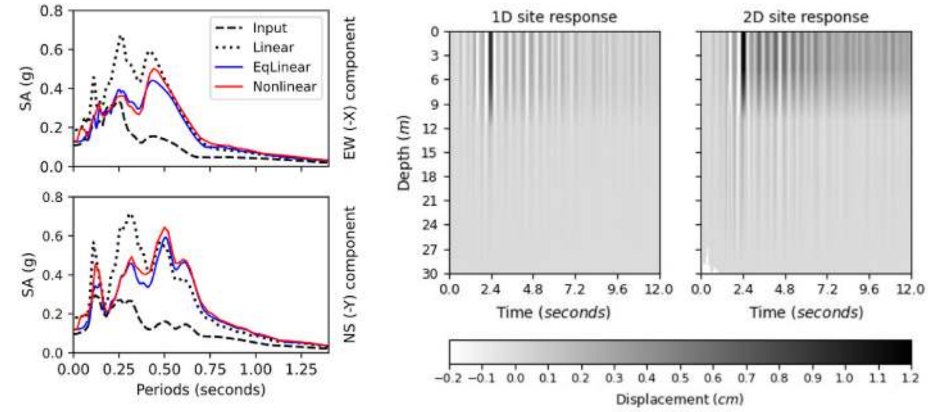

a) Spectral acceleration at free -surface b) 1D versus 2D inelastic site displacement contour plots

Fig. 7. a) 1D linear, equivalent-linear, and nonlinear site responses and b) residual displacement due to 2D slope slippage.

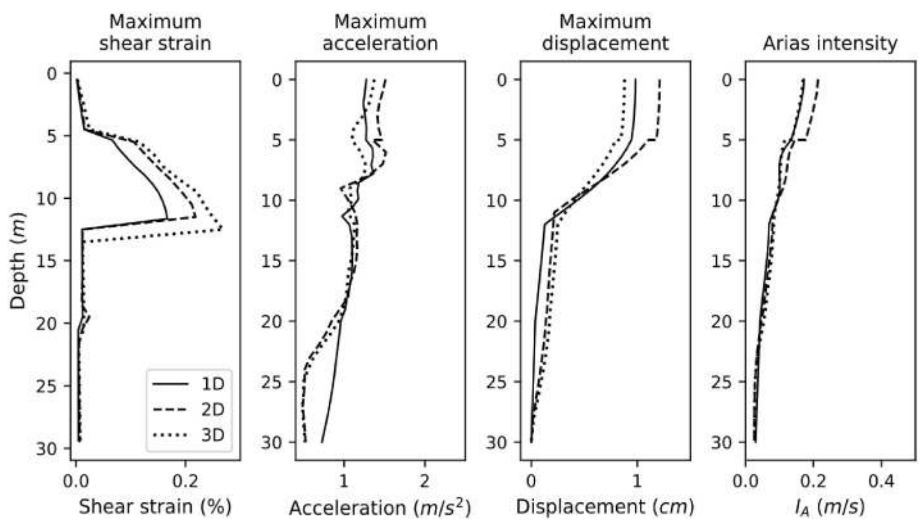

Fig. 8. Nonlinear 1D, 2D and 3D soil response profiles (Lazio-Abruzzo 1984 ground motion).

(EW, NS and UD) of the seismic event. The comparison among the 1D, 2D, and 3D soil-only models is used as a site-response consistency check for the input-motion implementation and boundary conditions adopted in the SFSI analyses. The 2D model produces the largest surface amplification (Fig. 8), whereas the 3D model exhibits lower horizontal peak surface displacements and larger vertical free-filed settlement, developing larger maximum shear strains. These differences are attributed to dimensional effects associated with the three-dimensional topography, transverse slope geometry, and finite-domain boundary conditions. At the tower location, however, the 3D model does not show suppression of residual vertical displacement; instead, it develops approximately 1.5 mm larger residual displacement than the corresponding 2D section model in the strong-slope direction. This difference is small relative to the 15-25 mm ratcheting-settlement range obtained in the nonlinear SFSI analyses (Section 3.4). Therefore, the 2D-3D differences in the soil-only analyses do not alter the main comparative trends associated with foundation cracking and nonlinear soil-structure interaction.

Finally, to verify that the adopted mesh accurately reproduces the frequency range of interest, the 2D model response is compared against a refined (1×1m) model (Fig. 9a). The combined effects of material strength reduction due to inelastic response and element size are expected to influence the resolution of higher frequencies. Ground motion is applied at the model base in two components: the EW component along the -X axis and the vertical (UD) component along the -Y axis. The acceleration field in the 3D contour plot remains continuous near the tower location and does not indicate significant boundary-induced distortion.

The proposed discretization of 3.6 m horizontal and 0.7 m vertical elements shows excellent agreement with the refined model in terms of acceleration histories and response spectra up to 18 Hz. Minor differences in ratcheting displacement (<6%) occur near the interface between the soft and medium clays due to localized slip, but these do not affect the overall response.

3.3. SFSI response and rocking isolation

Comparative dynamic analyses were performed for the fixed-base and direct soil-foundation-structure interaction (SFSI) models to quantify the influence of foundation flexibility, kinematic interaction and soil nonlinearity on the seismic response of the Guardiagrele bell tower. Both models share identical geometry, material properties, and consistent input ground motions to isolate the effects of soil–foundation interaction and the associated energy dissipation mechanisms within the soil.

In the fixed-base configuration, the free-surface motion from the 1D nonlinear site response analysis was applied directly at the base of the tower. In the SFSI model, the upward-propagating motion corresponding to the soil domain base depth (30 m) was applied as a force history at the model base, ensuring consistent three-component input for both analyses. Linear elastic simulations were also performed using the same

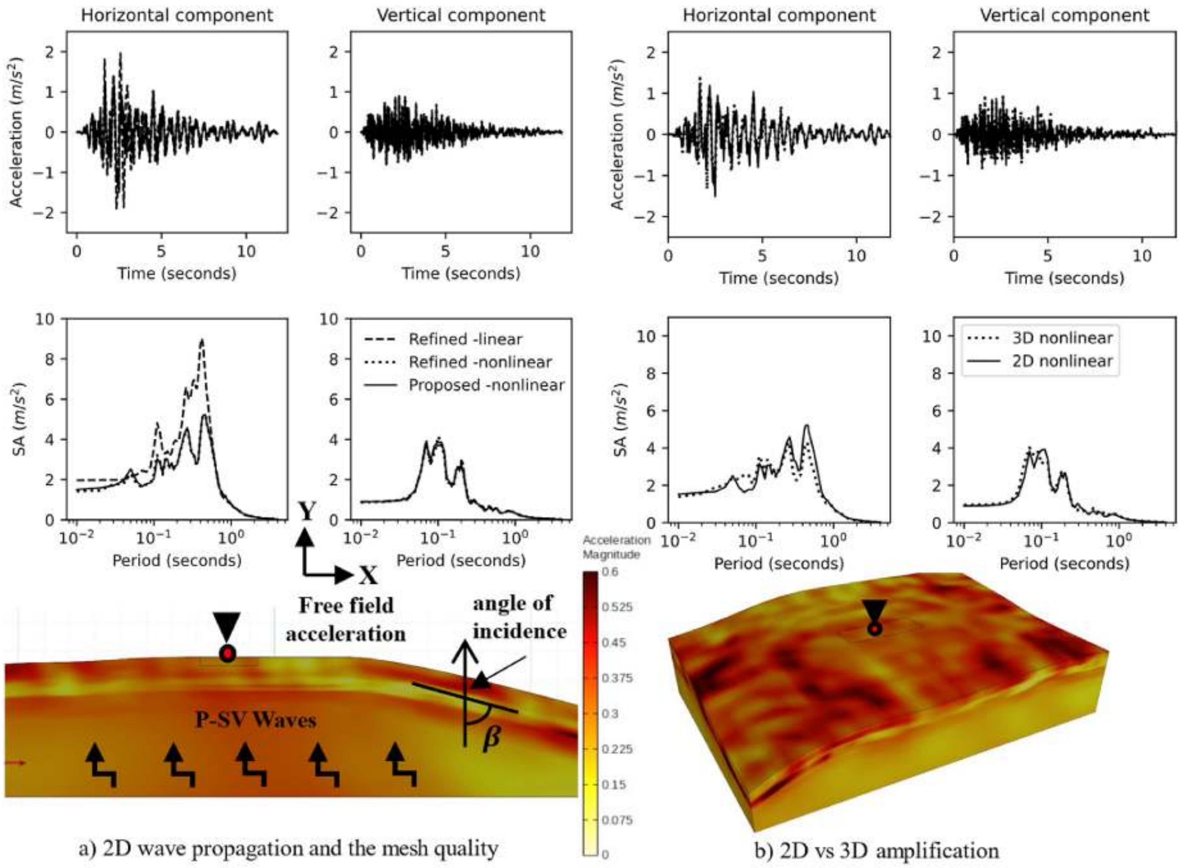

Fig. 9. a) Free-field acceleration spectra and mesh comparison indicating accurate frequency resolution and b) nonlinear displacements in 3D analysis.

configuration but employing motions from a 1D linear soil column. These reference analyses are used to separate the effects of structural nonlinearity and site-response assumptions from the additional effects introduced by foundation flexibility and full SFSI.

The acceleration histories recorded at the tower roof (Fig. 10) reveal a clear contrast in the dynamic behavior of the two systems. Under linear conditions, the fixed-base response is governed by the first structural mode of the tower, whereas the SFSI model is dominated by foundation rocking motion. The fundamental period in the EW direction increases from 0.28 to 0.29 s (fixed-base) to ≈ 0.44 s (SFSI), demonstrating the significant elongation introduced by elastic foundation compliance.

The foundation rotation angle, θ, can be calculated through two different approaches. The first approach derives θ from the differential vertical displacements recorded at the foundation corners, while the second estimates the base rotation from the relative roof displacement divided by the tower height, i.e., the roof drift ratio (RDR ≈ Δx/H). For small angles (i.e. geometrically linear analysis in OpenSees), RDR ≈ tan θ ≈ θ, and for a flexible tower, RDR ≈ θ + φ, where φ represents the structural deformation component. The close agreement between the computed rotations from both methods is shown in Fig. 11. This indicates that roof displacements primarily arise from foundation rotation, with structural deformations following the same phase pattern. It is worth noting that, early in the motion, when ground shaking intensity remains low, the tower behaves nearly as a rigid body, and the response is almost purely rotational.

It is worth noting that, the maximum computed foundation rotation

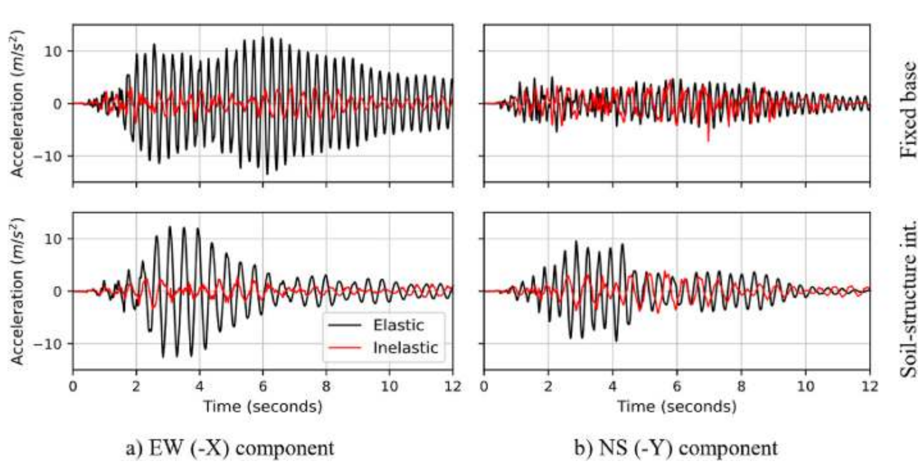

Fig. 10. Acceleration time histories recorded at the roof of the fixed-base and the SSI models.

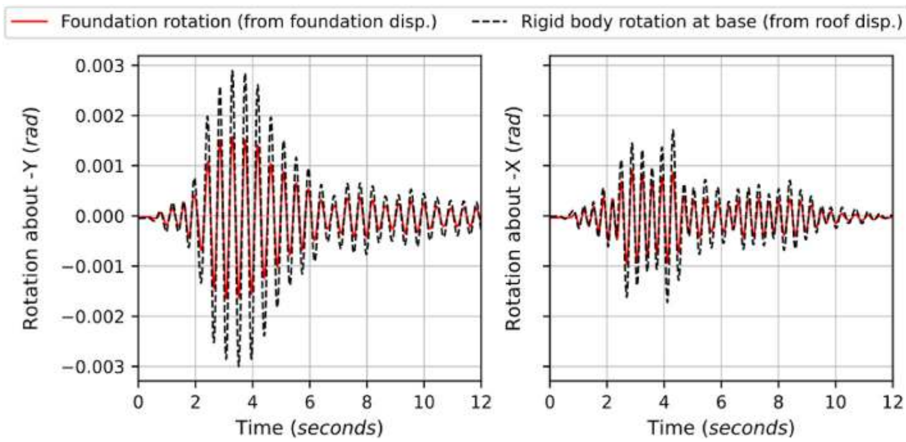

Fig. 11. Foundation rotation estimated from (1) corner displacements and (2) roof drift ratio (RDR = Δx/H).

was θmax $= 1.88 \times 10^{-3}$ rad (0.11°). At this rotation level, the small-rotation kinematic error is limited, with cos θ ≈ 1.000, and the associated P–Δ contribution remains small.

The frequency-domain amplification functions (Fig. 12) further support these findings. For the fixed-base model, the amplified frequencies align closely with the modal fundamental frequency of the structure (≈3.5 Hz in EW, ≈4.3 Hz in NS). In contrast, the SFSI system exhibits dominant peaks at a much lower frequency (≈2.73 Hz, T ≈ 0.35 s), near the soil column fundamental frequency. The fixed-base frequencies were identified from the roof/input transfer functions and cross-checked with the FE modal analysis summarized in Table 3, while the compliant-base frequencies were obtained from the dominant amplification peaks of the coupled SFSI transfer functions in Fig. 12b. This SFSI shifts the system's effective period to match the rocking–soil resonance rather than the first structural mode. In the second row, with increasing nonlinearity, the spectral peaks progressively flatten, reflecting hysteretic damping in both the masonry and the soil (see Table 4).

The fixed-base model shows clear frequency shift and reduced high-frequency content when material nonlinearity is considered, corresponding to damage-induced period elongation. The inelastic response is more pronounced in the NS direction due to the increased damage triggered by openings in the façade, which concentrate tensile strains and lead to the formation of a dominant diagonal cracking mechanism (Fig. 13a). In the SFSI model, however, the structural fundamental frequency is not as clearly identifiable in the transfer function (Fig. 12b). The absence of a distinct peak around T = 0.28 s does not imply that structural modes are inactive; instead, rocking-induced energy redistribution masks the structural contribution in the spectral domain. The final crack pattern in the SFSI model (Fig. 13a) suggests that the principal damage mode associated with the first structural period indeed develops along the NS axis, but with reduced intensity compared to the fixed-base configuration.

The coupled soil–foundation–structure model was checked against closed-form inertial-SSI theory in two complementary respects: period lengthening and system damping. The flexible-base fundamental period of the FE model ($\tilde{T}/T = 1.55$ and 1.66 in the EW and NS directions) reproduces, within 3–9% and with the same EW < NS ordering, three

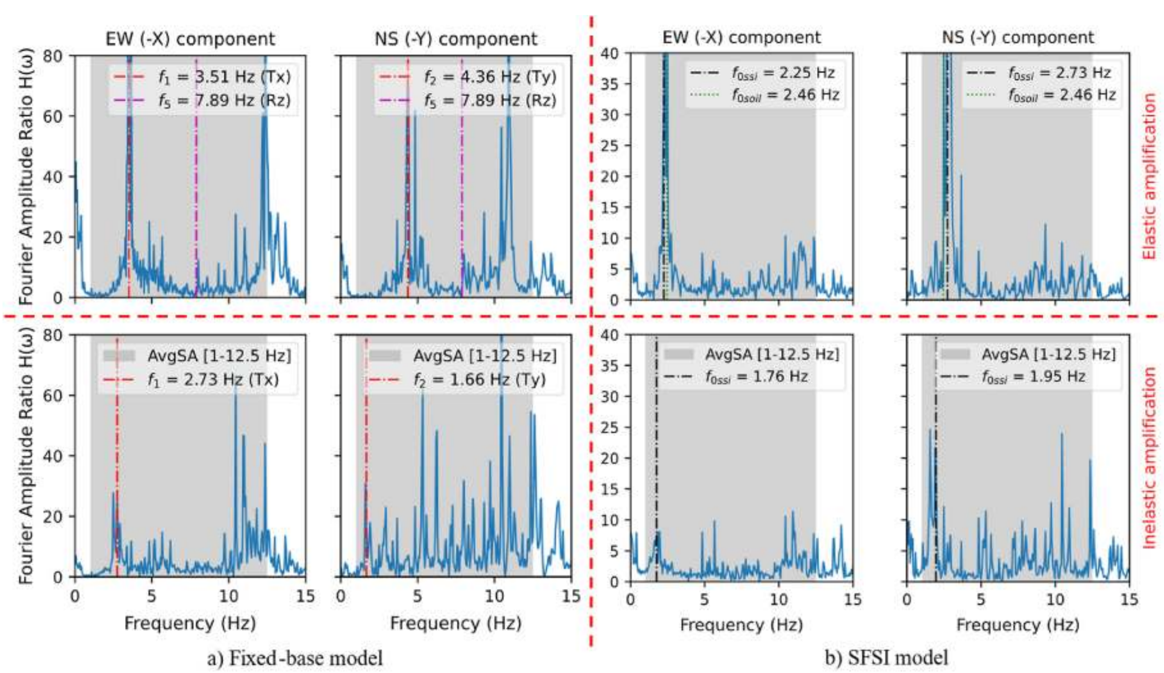

Fig. 12. Amplified frequencies computed at the roof of the bell tower. The vertical line is the fundamental frequency of the bell tower computed through the modal analysis. The shaded area marks the period range [0.08 - 1 s] included in the AvgSA definition.

Table 3
Comparison of ambient-vibration, FE modal analysis, and literature frequencies. Modes with mass participation below 0.5% are omitted.

Mode	Ambient Vibration	Modal Analysis	Mass Participation			Rosell (2010)	Camata et al. (2008)
	(***Hz***)	(***Hz***)	M_X(%)	M_Y(%)	R_Z(%)	(***Hz***)	(***Hz***)
1	3.45 - 4.07	3.52	55.14	-	-	3.33	3.78
2	6.95 – 7.44	4.35	-	65.34	-	3.65	3.93
5	7.95 – 8.45	7.88	-	-	52.75	7.37	8.53
6	10.04 – 11.56	11.01	-	12.72	-	10.11	11.85
7	13,70 – 15.16	12.40	20.422	-	-	12.25	13.32
8		13.36	2.23	-	0.79	13.05	14.86

Table 4
Parameters of the PressureDependendMultiYield material employed for the soil layers (in kN and m).

Parameter	Layer 1	Layer 2	Layer 3	Definition
rho	2.05	2.05	2.05	Density in tons per cubic meter
Gref	98,674	31,855	249,745	Shear modulus at Pref
Kref	953,856	307,934	2,414,203	Bulk modulus at Pref
cohesion	160	65	410	Shear strength at Pref (S_u)
ep	0.1	0.1	0.1	Strain at peak strength
Phi	0.0	0.0	0.0	Friction angle

independent analytical estimates the present sway–rocking closed-form solution (1.50/1.82), assembled from Ref. [82] surface impedances with [83] embedment factors, and the peer-reviewed dimensionless solution of [84] implemented in OD-In (1.47/1.77) reinforcing that the model captures the inertial period elongation expected for this foundation and soil.

The impact of material nonlinearity on seismic demand is quantified by studying the spectral acceleration comparison (Fig. 14) at the roof of the bell tower. Combinations of linear and nonlinear soil and structural models were analyzed to decouple the contribution of each source of energy dissipation. The inclusion of nonlinear soil behavior produces the most pronounced reduction in spectral acceleration, especially in the EW direction, where a substantial fraction of the input energy is dissipated by the hysteretic soil response. The difference between the linear-soil/nonlinear-structure and nonlinear-soil/linear-structure cases suggests that either nonlinear structure or nonlinear soil response can induce significant energy dissipation alone. When nonlinearity in both the masonry and the underlying soil is simultaneously accounted for, spectral amplitudes drop further, signifying an effective sharing of seismic energy in between structural cracking and foundation rocking.

Interestingly, in the NS direction, the linear-tower/nonlinear-soil and nonlinear-tower/linear-soil cases yield different roof response characteristics. A larger reduction and period elongation in tower response is observed when the soil nonlinear response is prevented. This is due to the strain softening response and increased damage in the tower due to a larger seismic demand than the linear-tower/nonlinear-soil case. The damage response observed in linear-tower/nonlinear-soil (Fig. 19) follows the cracking damage patterns computed in the fixed base model (Fig. 13a) which indicates comparable demands in both cases. The agreement between the roof spectra computed in nonlinear-tower/linear-soil, and nonlinear-tower/nonlinear-soil cases suggests that rocking isolation, rather than structural yielding, dominates the global energy dissipation mechanism. This indicates that even an elastic superstructure can benefit from the nonlinear deformation of the supporting soil, which acts as a natural isolator. This finding agrees with the rocking isolation phenomenon observed in RC structures by Ref. [1].

The resulting crack distributions at the end of ground shaking are shown in Fig. 13a. The fixed-base model develops extensive tensile damage in both directions, forming continuous diagonal cracks extending from openings to the tower base. In contrast, the SFSI model exhibits reduced damage intensity, with cracking localized near mid-height and at the base corners where rocking induces stress reversals.

The results are consistent with preliminary elastic-soil analyses by Ref. [19] which are shown in Fig. 13b [19]. reports a fully manifested failure mechanism along the tower in both fixed and SFSI models with limited differences. This aligns with the observation regarding the comparable demands induced by fixed and linear soil SFSI models. The failure planes in Ref. [19] occur in the vertical axis due to the isotropic damage-plasticity assumption by the author and fairly reproduced in

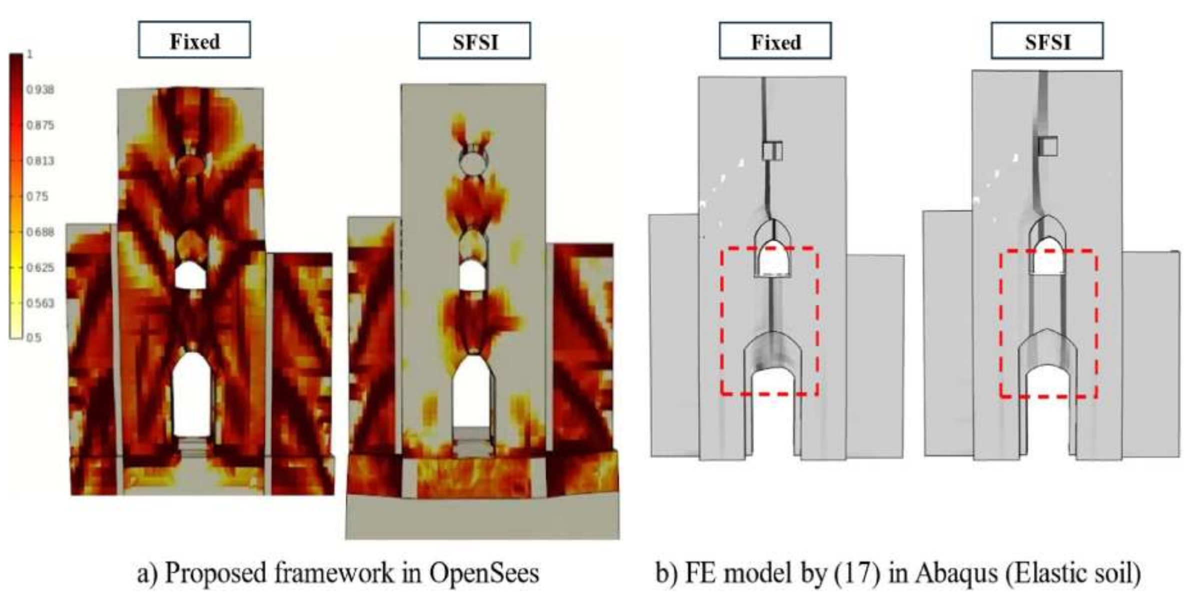

Fig. 13. Fixed-base versus SFSI damage patterns: a) Proposed framework, and b) as reported by [19].

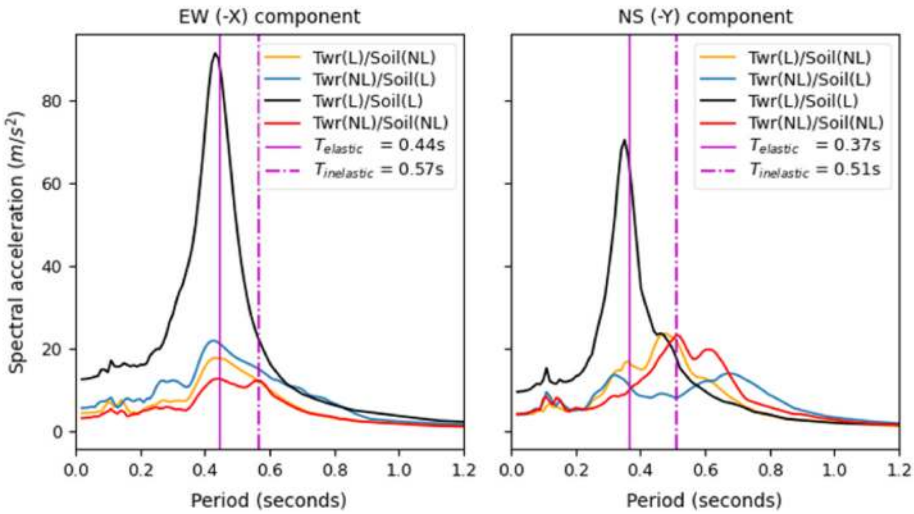

Fig. 14. Roof acceleration response spectra comparing combinations of linear and nonlinear soil and structural models.

Ref. [44] through isotropic analysis. The oblique crack planes in Fig. 13a are due to the orthotropic failure criteria in the ASDConcrete3D masonry model [44].

Overall, these results indicate that foundation rocking and soil nonlinearity strongly influence the global seismic response of the analyzed bell tower. The rocking isolation, previously reported for shallow-founded RC bridge piers and frame structures, is also observed in this squat masonry tower. The direct SFSI framework captures the coupling between soil yielding, foundation rotation, and masonry cracking, suggesting that neglecting soil–foundation interaction ay overestimate seismic demand and misrepresent the dominant deformation trend in this case.

3.4. Effect of soil nonlinearity on settlement and damage

The influence of foundation soil nonlinearity on the seismic response of the masonry tower is investigated through a series of multi-parametric analyses. To control the computational cost, a flat topography version of the model is used. The undrained strength, S_u and stiffness degradation characteristics of the upper soil layer are varied, while keeping the properties of deeper layers constant. These parameters govern the degree of energy dissipation and control the transfer of high-frequency acceleration to the superstructure. Fig. 15a presents the octahedral shear stress-strain backbones used for the analyses, with the 110 kPa case representing the reference response of the top clay layer. The 80 kPa and 50 kPa curves are derived by reducing γ_{peak} in the hyperbolic law shown in Eqn. (3.1). Since a is the same for all models, curves follow the degradation trend proposed by Ref. [48]. An additional case with the same undrained strength (110 kPa) but a slower degradation rate [50] is included to isolate the influence of the reduction law. The corresponding response spectra of the input motion are shown in Fig. 15b, highlighting the proximity of the tower's fundamental period to the predominant spectral peaks.

$$\frac{G}{G_{max}} = \frac{1}{1 + \left(\frac{\gamma}{\gamma_{peak}}\right)^{a}} \qquad 3.1$$

The resulting foundation settlements for different soil backbones are illustrated in Fig. 16. As expected, reducing S_u increases settlement magnitudes. However, the rate of stiffness degradation during ground shaking has a stronger effect on settlements than the magnitude of S_u. The [50] backbone has a long initial linear segment followed by an abrupt stiffness drop, transmits more high-frequency energy to the tower before yielding, resulting in smaller ground settlements. On the other hand [48], curves begin degrading at smaller strains; hence inducing larger settlements. In turn [48], curves transmit reduced high frequency demand to the tower as evidenced by the milder damage patterns observed in 50, 80, 110 kPa rows of Fig. 19.

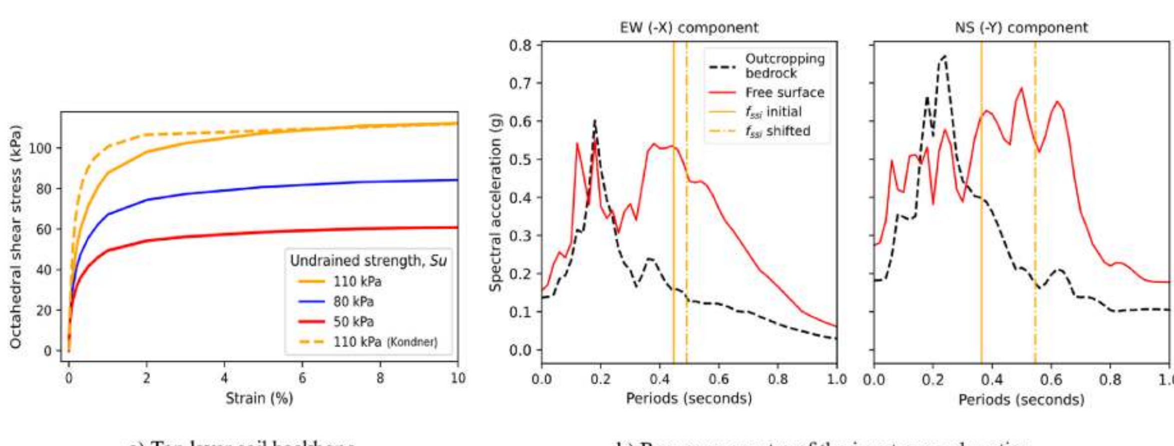

Fig. 15. Sensitivity analysis parameters a) the set of octahedral shear stress-strain curves, and b) response spectra of the input motion and the fundamental frequency of the bell tower.

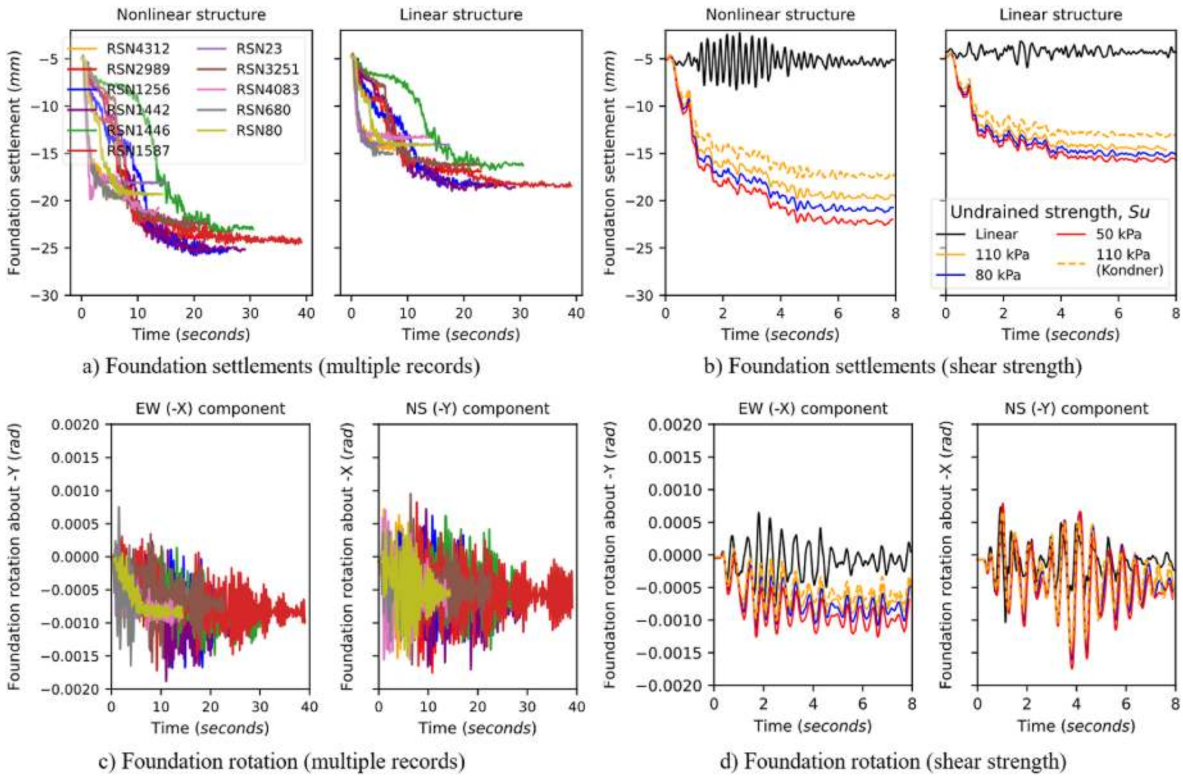

Fig. 16. Foundation settlement and rotation responses for nonlinear and linear structural models, showing record-to-record variability and sensitivity to undrained shear strength.

Conversely, the corresponding foundation rotations, shown in Fig. 16c and d, reveal greater sensitivity to soil strength than the settlement response. As S_u decreases, residual rotation about the global Y-axis (rocking direction) increases significantly, whereas rotation about the X-axis remains nearly unchanged due to the restraining effect of the adjacent walls. The larger foundation rotation at lower strengths reflects a transition from stiffness-controlled to inertia-controlled rocking, with greater energy dissipation in the foundation soil.

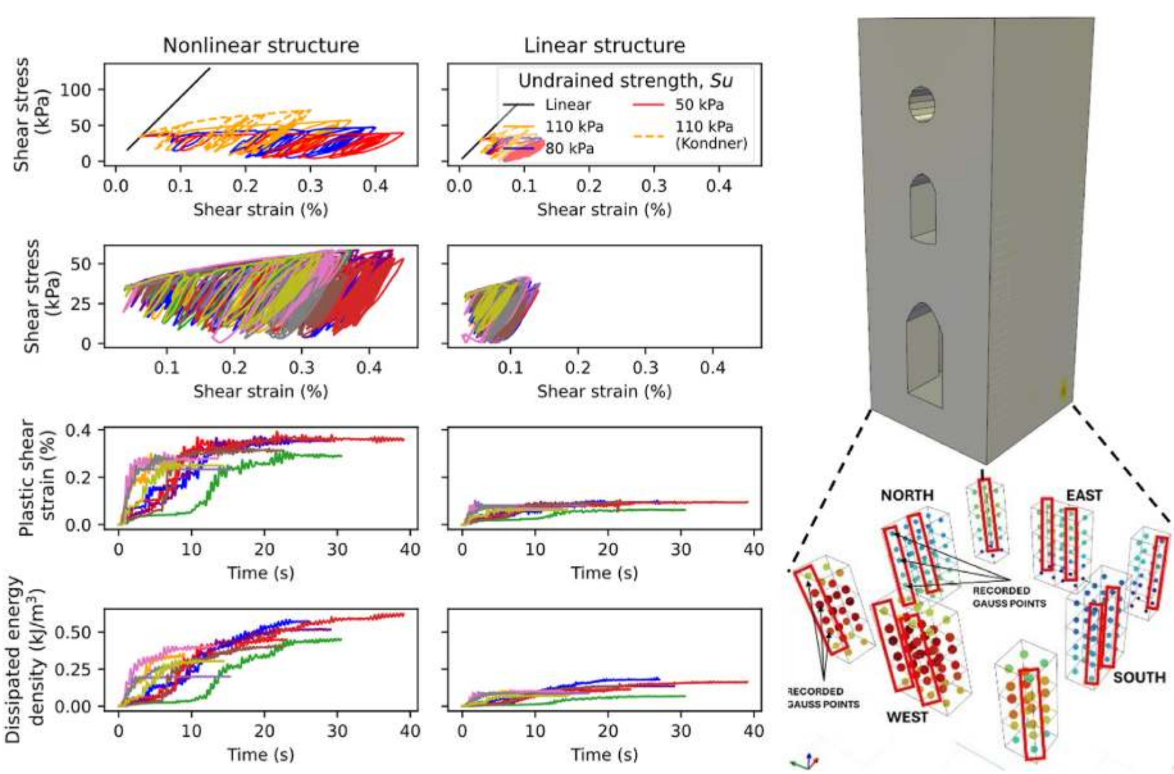

Fig. 17. Effect of undrained shear strength on the octahedral shear response of the north foundation-soil element under nonlinear and linear structural assumptions.

Interestingly, consistent higher settlements can be observed in Fig. 16, when the structure is nonlinear compared to when it remains elastic. This is due to the increased confining effect of the elastic foundation masonry on the foundation soil compared to the damaged foundation. It is worth noting that, undrained (volume-preserving) loading conditions are assumed in the analyses reported hereinafter. Therefore, deformations occur primarily through shear distortion and not due to volume changes in the foundation soil. Consequently, settlements originate from cyclic translation and rotation of soil elements. The confinement effect of the foundation masonry controls the shear deformations in the foundation soil, decreasing nonlinear soil response exhibited by the soil.

The eleven-record results in Fig. 16a–c indicate record-to-record variability in the amplitudes of settlement and foundation rotation, while preserving the same qualitative trend. The nonlinear structural model generally produces larger residual foundation deformation than the linear structural model, supporting the interpretation that foundation masonry damage reduces confinement and promotes nonlinear shear deformation in the soil. The suite is therefore used as a record-to-record consistency check, not as a probabilistic demand assessment.

Fig. 17 presents the octahedral stress–strain response of the soil elements surrounding the foundation. The transition from narrow, nearly elastic loops (stiff soil) to wide, dissipative hysteresis loops (soft soil) is evident. Allowing damage accumulation in the tower further amplifies soil strains and hysteresis loop areas, indicating strong coupling between superstructure cracking and soil nonlinearity. The increased tower flexibility induces larger horizontal displacements, promoting ratcheting-type cyclic shear distortions that accumulate as ratcheting settlement, even under constant-volume conditions. Cracking in the masonry foundation softens the load-transfer mechanism, reducing confinement pressures and allowing greater rocking-induced deformation in the surrounding soil.

The nonlinear soil models exhibit substantial reductions in base shear demand relative to the linear soil case, demonstrating the redistribution of seismic energy into foundation rocking and hysteretic soil deformation. The difference in peak demand among the nonlinear soil cases is modest, suggesting that once soil yielding initiates, further reductions in S_u have limited influence on peak force transmission.

The corresponding roof displacement orbits are shown in Fig. 18. The records produce different transient displacement paths, reflecting record-to-record variability in directionality and amplitude. However, the residual displacements remain limited and do not indicate a systematic one-directional drift of the tower. The mean residual roof displacement is small compared with the peak transient displacement range, supporting the interpretation that the main residual demand is concentrated at the foundation level through settlement and rotation rather than through permanent lateral drift of the superstructure.

The implications of these mechanisms are clearly visible in the cracking patterns illustrated in Fig. 19. When the foundation soil is forced to remain linear, the tower experiences severe tensile cracking concentrated around the openings and spandrels, as the full seismic demand is transferred to the structure. Introducing soil nonlinearity substantially reduces this damage by dissipating energy through foundation rocking and localized shear deformation. Nonetheless, the stiffness degradation law emerges as the governing factor: the [50] backbone, with its extended initial elastic range, allows greater high-frequency energy transmission before yielding, leading to more extensive cracking than the [48] law, which begins softening earlier. Thus, brittle masonry response is particularly sensitive to the width of the stiff part of the soil stress-strain curve. Wider linear regions

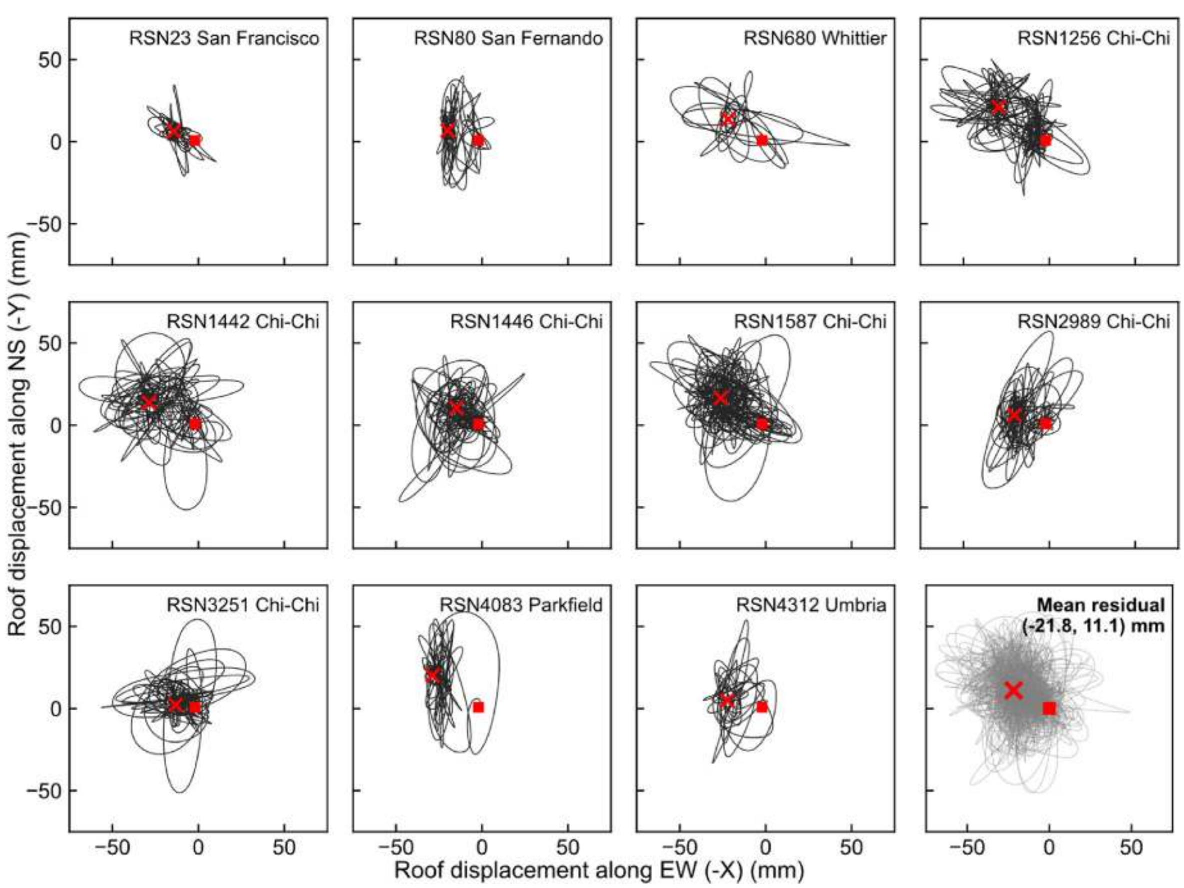

Fig. 18. Roof displacement orbits under the eleven selected records, showing transient and residual roof displacement in the horizontal plane. Red markers indicate residual displacements. (For interpretation of the references to colour in this figure legend, the reader is referred to the Web version of this article.)

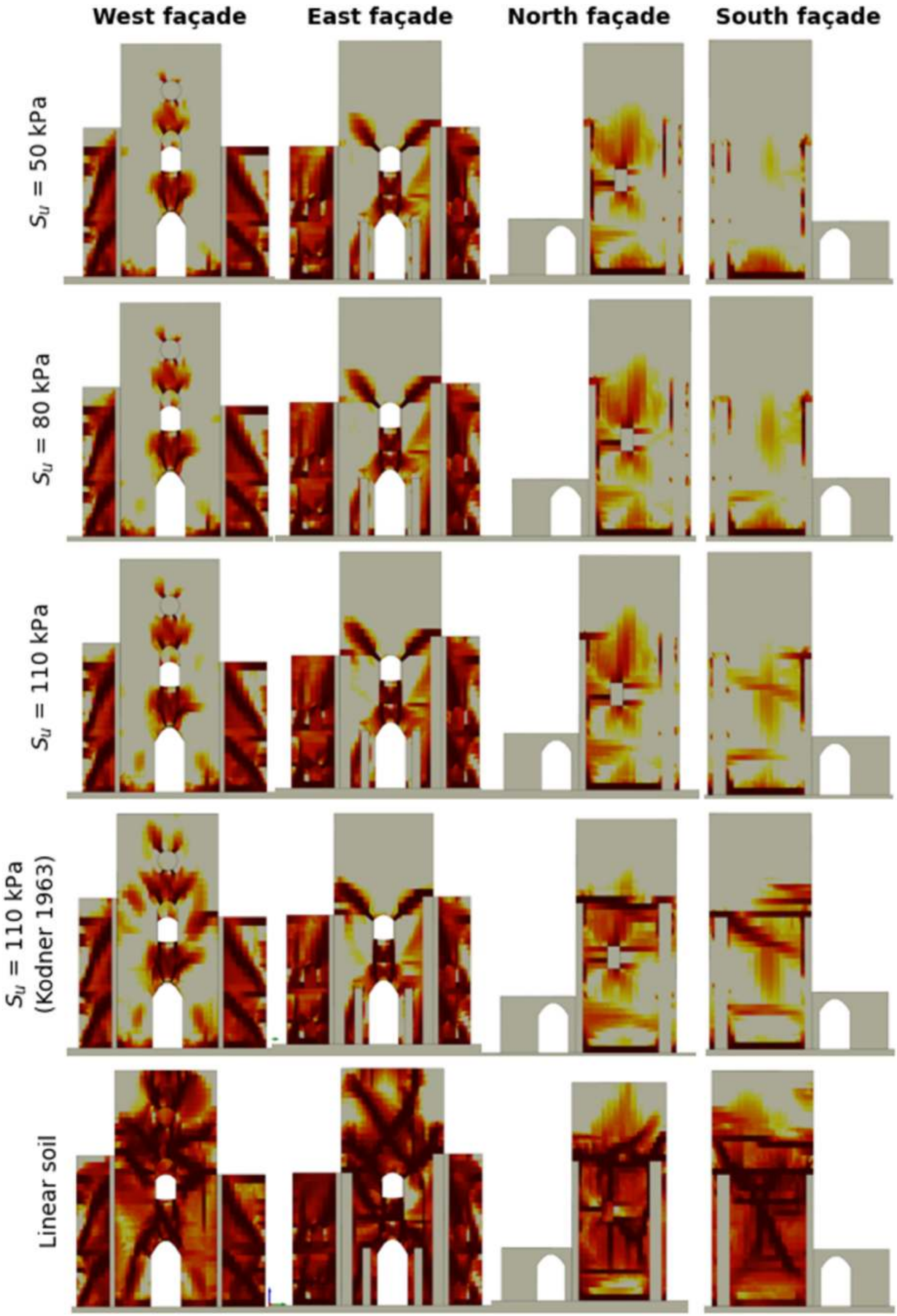

Fig. 19. Effect of soil strength on the tensile cracking damage patterns. Gauss points having a damage value between 0.5 and 1.0 are shown.

correspond to greater early-cycle acceleration transfer and higher damage accumulation.

Flexible-base damping was evaluated using the modular framework of [85]. The soil hysteretic component, βs, was obtained from the computed octahedral stress-strain loops of the foundation soil and ranged from 17% to 20% at the foundation edge elements. The radiation component, β*, was estimated using the OD-In analytical solution of [84], giving 2.0% in the EW direction and 2.6% in the NS direction. Combining these terms gives total flexible-base damping values of $\beta 0 \approx 13\%$ in the EW direction and $\beta 0 \approx 14\%$ in the NS direction. Soil hysteresis contributes about 80% of β0, radiation damping accounts for about 15-18%, and Rayleigh damping contributes only about 1%. Thus, foundation-soil hysteresis governs the flexible-base damping, while the adopted Rayleigh damping has influence only on the small strain wave-propagation.

The mesh-sensitivity results in Table 5 quantify the influence of the previously noted discretization dependence of accumulated soil plastic deformation on the tower response. The check was performed using a linear superstructure with nonlinear soil, so the reported variations isolate the effect of soil discretization. Peak roof acceleration is only moderately affected (0.60–0.74 g), and the soil dissipation remains stable for $h \leq 1.5$ m. In contrast, residual settlement decreases as the mesh is coarsened (−17.6 to −14.2 mm), while the 2.0 m mesh underrepresents soil dissipation. The 1.0 m mesh is therefore retained because it matches the soil calibration scale, avoids the reduced dissipation observed for the 2.0 m mesh, and keeps the computational cost feasible for the full nonlinear SFSI analyses.

Overall, the analyses demonstrate that foundation soil nonlinearity can significantly mitigate seismic demand and reduce masonry damage through energy dissipation mechanisms. However, this beneficial effect depends critically on the form of the stiffness degradation law, not solely on soil strength. Rapid stiffness degradation, as in Ref. [48], provides early isolation and limits high-frequency transmission, while delayed degradation, as in Ref. [50], increases early-cycle excitation and accelerates damage formation. These findings align with the “rocking isolation” concept observed in shallow-founded reinforced concrete structures [1], [2], [3], now extended here to masonry towers. Future research could further examine the influence of soil heterogeneity and foundation size, as these may introduce differential settlements and localized damage amplification in tall, slender masonry structures.

4. Concluding remarks

This study presented a high-fidelity nonlinear finite element framework for direct simulation of soil–shallow foundation–structure interaction (SFSI) in masonry towers, integrating anisotropic damage–plasticity modeling for masonry structures, multi-yield plasticity stress-strain law for soils, and frictional contact interfaces within OpenSees. The mixed implicit–explicit (IMPL-EX) material-integration scheme was employed to achieve robust and computationally efficient nonlinear dynamic analyses, enabling stable solutions for large-scale coupled soil–masonry systems. The framework was applied on a shallow-founded stone masonry bell tower of the Cathedral of Santa Maria Maggiore in Guardiagrele, Italy. The results indicate that foundation rocking and soil nonlinearity govern the seismic response of the analyzed squat tower, controlling both period elongation and the distribution of structural damage.

The analyses indicate that nonlinear foundation rotation reduces the seismic demand of the tower in the analyzed configuration, reducing the roof accelerations and cracking damage patterns. The rate of shear modulus degradation in the foundation soil is found to be a key factor in seismic energy transfer. When stiffness degradation initiates early at small strains, the soil dissipates a significant portion of input energy through hysteretic response, filtering high-frequency accelerations and mitigating masonry cracking. Conversely, slower stiffness loss, even at the same undrained soil shear strength, delays yielding and transmit more high-frequency energy before softening, thereby increasing cracking severity.

As observed by Ref. [1] in RC structures, the benefits of rocking isolation in reducing cracking damage surpass the adverse impacts of settlement also in historical masonry towers. Once the foundation masonry cracks, its stiffness and confinement capacity on the foundation soil decreases, amplifying rocking and nonlinear shear distortions in the soil. This feedback mechanism decreases the overall structural demand at the cost of accelerated settlement accumulation. This illustrates the dual nature of rocking isolation-beneficial mechanism for reducing lateral forces, yet potentially detrimental due to co-seismic foundation deformation. However, it is worth noting that, in all cases (Fig. 16c) residual rotations remain below the 1/500 serviceability threshold specified in the design code [86]. As observed by Ref. [1] in RC structures, the benefits of rocking isolation in reducing cracking damage surpass the adverse impacts of settlement also in historical masonry towers.

The key contributions of this study can be summarized as follows:

- Integration of a direct 3D nonlinear SFSI model in OpenSees combining damage–plasticity modeling for masonry structures, multi-yield soil plasticity stress-strain law, and contact interfaces within the OpenSees/STKO environment.
- Identification, for the analyzed case, of the role of foundation rocking and shear modulus degradation rate in controlling high-frequency energy transmission and damage evolution in shallow-founded masonry structures.
- Observation of a coupled response trend linking foundation cracking, soil nonlinearity, and accelerated ratcheting settlement accumulation in the analyzed soil-structure system.

Nevertheless, several limitations remain:

- The current analyses exclude geometric nonlinear effects. This limitation is expected to be less critical for the targeted class of squat masonry towers and similar squat structures, where rocking rotations generally remain small; however, it may become important for taller or more slender structures and for larger-deformation response, where P–Δ effects can amplify demand and reduce stability margins.
- The assumed uniform S_u profile may oversimplify the real foundation response. Future studies should account for depth-dependent S_u to better represent layered or heterogeneous fine-grained soil deposits.
- The analyses are performed within a total-stress undrained formulation. Therefore, the computed vertical foundation displacements are interpreted as co-seismic ratcheting settlement accumulated during cyclic loading, together with residual foundation rotation at the end of shaking. They should not be interpreted as long-term consolidation settlement or as deformation caused by excess pore-pressure generation, effective-stress degradation, cyclic mobility, liquefaction, or post-shaking reconsolidation.
- The adopted multi-yield soil constitutive model does not capture strain-softening effects typical of structured or cemented clays;

Table 5
Mesh-sensitivity check for settlement, roof acceleration, and soil dissipation. The dissipation is normalized stress–strain loop area; larger values indicate greater soil energy loss.

Mesh size (m)	Residual settlement (mm)	Peak roof acceleration (g)	Soil energy dissipation (normalized)
0.5	−17.6	0.61	0.90
0.8	−16.5	0.60	0.95
1.0	−15.8	0.61	1.00
1.5	−14.5	0.74	0.95
2.0	−14.2	0.67	0.36

including these behaviors would improve predictions of post-peak response and settlement accumulation.

Beyond providing physical insight, this study also shows that the IMPL-EX material-integration scheme can make this class of nonlinear direct SFSI simulations computationally tractable for large-scale nonlinear SFSI analyses, providing stable convergence with minimal computational overhead. The IMPL-EX algorithm was instrumental in enabling extensive sensitivity analyses and in sustaining nonlinear simulations even after severe cracking in the fixed-base and linear-soil cases. However, the method is only conditionally stable, and the robustness of the results should not be taken for granted. The time-step assessment indicated (Table 1) that using the seismic record's sampling interval was sufficient to capture the tower response for the 475-year return period motions considered here. Overall, the IMPL-EX formulation proved highly effective in capturing the SFSI response while substantially reducing computational cost. By enabling stable and efficient nonlinear dynamic simulations, the proposed framework offers a practical and scalable tool for the seismic assessment of masonry and other brittle structures, providing an efficient framework for incorporating direct soil–foundation–structure interaction into performance-based evaluation and design.

Funding statement

The work presented in this paper was carried out initially at the IUSS Pavia as part of the first author's PhD work and continued at the University of Chieti-Pescara thanks to a fellowship funded by Project STRIC - Centro internazionale per la ricerca sulle Scienze e tecniche della ricostruzione fisica, economica e sociale, PNC - Piano Nazionale Complementare al PNRR - PNC Sisma. Sub-misura 84 "Centri di ricerca per l'innovazione", linea di intervento n. 1 "Contributo per la realizzazione e/o implementazione di 4 centri di ricerca e trasferimento tecnologico". Funding by both institutions is greatly appreciated.

CRediT authorship contribution statement

Onur Deniz Akan: Conceptualization, Formal analysis, Investigation, Methodology, Software, Validation, Visualization, Writing – original draft. **Massimo Petracca:** Conceptualization, Resources, Software, Writing – review & editing. **Guido Camata:** Conceptualization, Methodology, Resources, Software, Supervision. **Carlo G. Lai:** Methodology, Project administration, Supervision, Writing – review & editing. **Enrico Spacone:** Funding acquisition, Methodology, Project administration, Supervision, Writing – review & editing. **Claudio Tamagnini:** Methodology, Supervision, Writing – review & editing.

Declaration of competing interest

The authors declare that they have no known competing financial interests or personal relationships that could have appeared to influence the work reported in this paper.

Acknowledgements

The authors gratefully acknowledge Dr. Ali Güney Özcebe for providing valuable technical insights into site response analysis and 3D geotechnical modelling in OpenSees for nonlinear dynamic analysis. The authors also thank Mr. Luis Rosell for his Master’s thesis, which provided useful background and implementation insights relevant to the present work.

Data availability

Data will be made available on request.

References

[1] Gazetas G. 4th Ishihara lecture: Soil–foundation–structure systems beyond conventional seismic failure thresholds. Soil Dynam Earthq Eng Jan. 2015;68: 23–39. https://doi.org/10.1016/j.soildyn.2014.09.012.

[2] Gelagoti F, Kourkoulis R, Anastasopoulos I, Gazetas G. Rocking-isolated frame structures: margins of safety against toppling collapse and simplified design approach. Soil Dynam Earthq Eng Jan. 2012;32(1). https://doi.org/10.1016/j.soildyn.2011.08.008. Art. no. 1.

[3] Anastasopoulos I, Gazetas G, Loli M, Apostolou M, Gerolymos N. Soil failure can be used for seismic protection of structures. Bull Earthq Eng 2010;8:309–26.

[4] Kausel E. Early history of soil–structure interaction. Soil Dynam Earthq Eng Sep. 2010;30(9). https://doi.org/10.1016/j.soildyn.2009.11.001. Art. no. 9.

[5] Kausel E, Whitman RV, Morray JP, Elsabee F. The spring method for embedded foundations. Nucl Eng Des Aug. 1978;48(2):377–92. https://doi.org/10.1016/0029-5493(78)90085-7.

[6] Huang S, Ozcelik O, Gu Q. A practical and efficient coupling method for large scale soil–structure interaction problems. Soil Dynam Earthq Eng Sep. 2015;76:44–57. https://doi.org/10.1016/j.soildyn.2014.12.014.

[7] Mylonakis G, Nikolaou S, Gazetas G. Footings under seismic loading: analysis and design issues with emphasis on bridge foundations. Soil Dynam Earthq Eng Sep. 2006;26(9):824–53. https://doi.org/10.1016/j.soildyn.2005.12.005.

[8] Chatzigogos CT, Pecker A, Salençon J. Macroelement modeling of shallow foundations. Soil Dynam Earthq Eng May 2009;29(5):765–81. https://doi.org/10.1016/j.soildyn.2008.08.009.

[9] Cremer C, Pecker A, Davenne L. Modelling of nonlinear dynamic behaviour of a shallow strip foundation with macro-element. J Earthq Eng Apr. 2002;6(2): 175–211. https://doi.org/10.1080/13632460209350414.

[10] Gajan S, Kutter B. A contact interface model for nonlinear cyclic moment-rotation behavior of shallow foundations. Presented at the 4th international conference on earthquake geotechnical engineering, Thessaloniki, Greece. Jun. 2007.

[11] Taciroglu E, Rha C, Wallace JW. A robust macroelement model for soil–pile interaction under cyclic loads. J Geotech Geoenviron Eng Oct. 2006;132(10): 1304–14. https://doi.org/10.1061/(ASCE)1090-0241(2006)132:10(1304).

[12] Lai CG, Martinelli M. Soil-structure interaction under earthquake loading: theoretical framework. In: *ALERT doctoral school 2013 soil-structure interaction*, the alliance of laboratories in Europe for research and technology; 2013. p. 3–43.

[13] Romero-Sánchez E, Requena-Garcia-Cruz M-V, Morales-Esteban A. Impact of the soil-foundation-structure interaction in the seismic behaviour of a heritage masonry tower: the giralda of Seville. Eng Fail Anal Sep. 2024;163:108580. https://doi.org/10.1016/j.engfailanal.2024.108580.

[14] Zeolla E, Brunelli A, de Silva F, Cattari S, Sica S. Fragility curves of URM buildings in aggregate considering the interaction with soil and among nearby footings. Bull Earthq Eng Jul. 2025;23(9):3589–622. https://doi.org/10.1007/s10518-025-02178-x.

[15] Lancellotta R, Sabia D. Identification technique for soil-structure analysis of the ghirlandina tower. Int J Architect Herit May 2015;9(4):391–407. https://doi.org/10.1080/15583058.2013.793438.

[16] de Silva F, Ceroni F, Sica S, Silvestri F. Non-linear analysis of the Carmine bell tower under seismic actions accounting for soil–foundation–structure interaction. Bull Earthq Eng Jul. 2018;16(7). https://doi.org/10.1007/s10518-017-0298-0. Art. no. 7.

[17] Chinmayi HK. Study on pounding of structures with soil–structure interaction effects: a review. J Inst Eng India Ser A Mar. 2019;100(1):199–204. https://doi.org/10.1007/s40030-018-0341-4.

[18] Castelli F, Grasso S, Lentini V, Sammito MSV. Nonlinear 3D finite element analysis of a coupled soil–structure system by a deterministic approach. Geosciences Apr. 2024;14(4):100. https://doi.org/10.3390/geosciences14040100.

[19] Rosell LA. Explicit/implicit nonlinear soil structure interaction study of the bell tower of Santa Maria maggiore , guardiagrele. Istituto Universitario di Studi Superiori di Pavia; 2010.

[20] Camata G, Cifelli L, Spacone E, Conte J, Torrese P. Safety analysis of the bell tower of St. Maria maggiore cathedral in guardiagrele (Italy). In: The 14th world conference on earthquake engineering; 2008. https://doi.org/10.4203/ccp.88.58.

[21] Casolo S, Diana V, Uva G. Influence of soil deformability on the seismic response of a masonry tower. Bull Earthq Eng May 2017;15(5):1991–2014. https://doi.org/10.1007/s10518-016-0061-y.

[22] Casolo S, Milani G, Uva G, Alessandri C. Comparative seismic vulnerability analysis on ten masonry towers in the coastal Po Valley in Italy. Eng Struct Apr. 2013;49: 465–90. https://doi.org/10.1016/j.engstruct.2012.11.033.

[23] Bullock Z, Dashti S, Karimi Z, Liel A, Porter K, Franke K. Probabilistic models for residual and peak transient tilt of mat-founded structures on liquefiable soils. J Geotech Geoenviron Eng 2019;145(2):04018108. https://doi.org/10.1061/(asce)gt.1943-5606.0002002.

[24] Bray JD, Macedo J. 6th Ishihara lecture: simplified procedure for estimating liquefaction-induced building settlement. Soil Dynam Earthq Eng 2017;102 (September):215–31. https://doi.org/10.1016/j.soildyn.2017.08.026.

[25] Elgamal A, Yan L, Yang Z, Conte JP. Three-dimensional seismic response of humboldt Bay bridge-foundation-ground system. J Struct Eng 2008;134(7): 1165–76. https://doi.org/10.1061/(asce)0733-9445(2008)134:7(1165).

[26] Khosravifar A, Elgamal A, Lu J, Li J. A 3D model for earthquake-induced liquefaction triggering and post-liquefaction response. Soil Dynam Earthq Eng 2018;110. https://doi.org/10.1016/j.soildyn.2018.04.008. April, Art. no. April.

[27] Qiu Z, Lu J, Elgamal A, Su L, Wang N, Almutairi A. OpenSees three-dimensional computational modeling of ground structure systems and liquefaction scenarios.

CMES - Comput Model Eng Sci 2019;120(3). https://doi.org/10.32604/cmes.2019.05759. Art. no. 3.
[28] Petalas AL, Dafalias YF, Papadimitriou AG. SANISAND-F: sand constitutive model with evolving fabric anisotropy. Int J Solid Struct Apr. 2020;188–189:12–31. https://doi.org/10.1016/j.ijsolstr.2019.09.005.
[29] Manzari MT, Dafalias YF. A critical state two-surface plasticity model for sands. Geotechnique Apr. 1997;47(2). https://doi.org/10.1680/geot.1997.47.2.255. Art. no. 2.
[30] Boulanger RW, Ziotopoulou K. PM4SAND (VERSION 3.2): A sand plasticity model for earthquake engineering applications. Davis, CA: UNIVERSITY OF CALIFORNIA AT DAVIS; 2022.
[31] Mróz Z. On the description of anisotropic workhardening. J Mech Phys Solid May 1967;15(3):163–75. https://doi.org/10.1016/0022-5096(67)90030-0.
[32] Mróz Z, Pietruszczak St. A constitutive model for sand with anisotropic hardening rule. Int J Numer Anal Methods GeoMech 1983;7(3):305–20. https://doi.org/10.1002/nag.1610070304.
[33] Prevost JH. DYNA1D: a computer program for nonlinear seismic site response analysis - technical documentation. Princeton, NJ: Princeton University; Sep. 1989. NCEER-89-0025.
[34] Yang Z, Elgamal A, Parra E. Computational model for cyclic mobility and associated shear deformation. J Geotech Geoenviron Eng Dec. 2003;129(12): 1119–27. https://doi.org/10.1061/(ASCE)1090-0241(2003)129:12(1119).
[35] Yang Z, Elgamal A. Multi-surface cyclic plasticity sand model with lode angle effect. Geotech Geol Eng Jun. 2008;26(3):335–48. https://doi.org/10.1007/s10706-007-9170-3.
[36] Elgamal A, Yang Z, Parra E, Ragheb A. Modeling of cyclic mobility in saturated cohesionless soils. Int J Plast Jun. 2003;19(6):883–905. https://doi.org/10.1016/S0749-6419(02)00010-4.
[37] Gu Q, Conte JP, Elgamal A, Yang Z. Finite element response sensitivity analysis of multi-yield-surface J2 plasticity model by direct differentiation method. Comput Methods Appl Mech Eng Jun. 2009;198(30):2272–85. https://doi.org/10.1016/j.cma.2009.02.030.
[38] Gu Q, Conte JP, Yang Z, Elgamal A. Consistent tangent moduli for multi-yield-surface J2 plasticity model. Comput Mech Jul. 2011;48(1):97–120. https://doi.org/10.1007/s00466-011-0576-7.
[39] Gu Q, Qiu Z, Huang S. A modified multi-yield-surface plasticity model: sequential closest point projection method. Comput Geotech Sep. 2015;69:378–95. https://doi.org/10.1016/j.compgeo.2015.05.020.
[40] Qiu Z, Elgamal A. Three-dimensional modeling of strain-softening soil response for seismic-loading applications. J Geotech Geoenviron Eng Jul. 2020;146(7). https://doi.org/10.1061/(ASCE)GT.1943-5606.0002282. Art. no. 7.
[41] Tu X, Andrade JE, Chen Q. Return mapping for nonsmooth and multiscale elastoplasticity. Comput Methods Appl Mech Eng Jun. 2009;198(30). https://doi.org/10.1016/j.cma.2009.02.014. Art. no. 30.
[42] Oliver J, Huespe AE, Cante JC. An implicit/explicit integration scheme to increase computability of non-linear material and contact/friction problems. Comput Methods Appl Mech Eng 2008;197(21–24):1865–89. https://doi.org/10.1016/j.cma.2007.11.027.
[43] Petracca M, Camata G, Spacone E, Pelà L. Efficient constitutive model for continuous micro-modeling of masonry structures. Int J Architect Herit Sep. 2022; 0(0):1–13. https://doi.org/10.1080/15583058.2022.2124133.
[44] Akan OD. 3D numerical investigation of nonlinear seismic soil-structure interaction in shallow-founded masonry towers with mixed implicit-explicit integration for improved solution stability. Pavia: Scuola Universitaria Superiore IUSS Pavia; 2024. PhD Thesis.
[45] Mazzoni S, Mckenna F, Scott MH, Fenves GL. OpenSees command language manual. 2006.
[46] Petracca M, Candeloro F, Camata G, Scientific Toolkit for OpenSees (STKO) user manual. ASDEA software technology, Pescara, Italy. 2017.
[47] McGann CR, Arduino P, Mackenzie-Helnwein P. A stabilized single-point finite element formulation for three-dimensional dynamic analysis of saturated soils. Comput Geotech May 2015;66:126–41. https://doi.org/10.1016/j.compgeo.2015.01.002.
[48] Vucetic M, Dobry R. Effect of soil plasticity on cyclic response. J Geotech Eng Jan. 1991;117(1):89–107. https://doi.org/10.1061/(ASCE)0733-9410(1991)117:1(89).
[49] Wichtmann T, Triantafyllidis T. Monotonic and cyclic tests on kaolin: a database for the development, calibration and verification of constitutive models for cohesive soils with focus to cyclic loading. Acta Geotech Oct. 2018;13(5):1103–28. https://doi.org/10.1007/s11440-017-0588-3.
[50] Kondner RL. Hyperbolic stress-strain response: cohesive soils. J Soil Mech Found Div Feb. 1963;89(1). https://doi.org/10.1061/JSFEAQ.0000479. Art. no. 1.
[51] Seed HB, Idriss IM. Soil moduli and damping factors for dynamic response analyses. California Univ., Berkeley. Earthquake engineering research Center. 1970. PB197869, https://ntrl.ntis.gov/NTRL/dashboard/searchResults/titleDetail/PB197869.xhtml. [Accessed 13 December 2023].
[52] Darendeli MB. Development of a new family of normalized modulus reduction and material damping curves. The University of Texas at Austin; 2001. PhD Thesis.
[53] Das BM. Advanced soil mechanics, fifth edition. Boca Raton London New York: CRC Press; 2020.
[54] Kanellopoulos C, Rangelow P, Jeremic B, Anastasopoulos I, Stojadinovic B. Dynamic structure-soil-structure-interaction for nuclear power plants. arXiv: arXiv: 231010251 Oct. 16, 2023. https://doi.org/10.48550/arXiv.2310.10251.
[55] Anastasopoulos I, Gelagoti F, Kourkoulis R, Gazetas G. Simplified constitutive model for simulation of cyclic response of shallow foundations: validation against laboratory tests. J Geotech Geoenviron Eng Dec. 2011;137(12):1154–68. https://doi.org/10.1061/(ASCE)GT.1943-5606.0000534.
[56] Potts DM, Zdravkovic L. Finite element analysis in geotechnical engineering: theory. Thomas Telford; 1999.
[57] Hallal MM, Cox BR. An H/V geostatistical approach for building pseudo-3D Vs models to account for spatial variability in ground response analyses Part I: model development. Earthq Spectra Aug. 2021;37(3):2013–40. https://doi.org/10.1177/8755293020981989.
[58] Coleman J, Spacone E. Localization issues in force-based frame elements. J Struct Eng Nov. 2001;127(11):1257–65. https://doi.org/10.1061/(ASCE)0733-9445(2001)127:11(1257).
[59] Lysmer J, Kuhlemeyer RL. Finite dynamic model for infinite media. J Eng Mech Div Aug. 1969;95(4):859–77. https://doi.org/10.1061/JMCEA3.0001144.
[60] Nielsen AH. Absorbing boundary conditions for seismic analysis in ABAQUS. In: ABAQUS users' conference; 2006. p. 359–76.
[61] Su L, et al. Seismic fragility analysis of pile-supported wharves with the influence of soil permeability. Soil Dynam Earthq Eng Jul. 2019;122:211–27. https://doi.org/10.1016/j.soildyn.2019.04.003.
[62] Bielak J, Loukakis K, Hisada Y, Yoshimura C. Domain reduction method for three-dimensional earthquake modeling in localized regions, part I: theory. Bull Seismol Soc Am 2003;93(2):817–24. https://doi.org/10.1785/0120010251.
[63] Yoshimura C, Bielak J, Hisada Y, Fernández A. Domain reduction method for three-dimensional earthquake modeling in localized regions, part II: verification and applications. Bull Seismol Soc Am 2003;93(2):825–40. https://doi.org/10.1785/0120010252.
[64] Zhang W, Seylabi EE, Taciroglu E. An ABAQUS toolbox for soil-structure interaction analysis. Comput Geotech Oct. 2019;114:103143. https://doi.org/10.1016/j.compgeo.2019.103143.
[65] Abell JA, Orbović N, McCallen DB, Jeremic B. Earthquake soil-structure interaction of nuclear power plants, differences in response to 3-D, 3 × 1-D, and 1-D excitations. Earthq Eng Struct Dynam May 2018;47(6). https://doi.org/10.1002/eqe.3026. Art. no. 6.
[66] Abell JA, Crempien JG, Recabarren M. ShakerMaker: a framework that simplifies the simulation of seismic ground-motions. SoftwareX 2022;17:100911.
[67] Lu J, Elgamal A, Law KH, Yang Z. Parallel computing for seismic geotechnical applications. Apr. 2012. p. 1–6. https://doi.org/10.1061/40803(187)182.
[68] McKenna FT. "Object-oriented finite element programming: frameworks for analysis. Algorithms and parallel computing. Berkeley: University of California; 1997.
[69] Mckenna F, Fenves GL. TN-2007-16 using the OpenSees interpreter on parallel computers. 2007. p. 1–15.
[70] Amestoy PR, Duff IS, L'Excellent J-Y, Koster J. A fully asynchronous multifrontal solver using distributed dynamic scheduling. SIAM J Matrix Anal Appl Jan. 2001; 23(1):15–41. https://doi.org/10.1137/S0895479899358194.
[71] Biondi S, Camata G, Candigliota E, Spacone E, Valente C. Identificazione strutturale di una torre in muratura per la messa a punto del modello numerico. Presented at the XIII Convegno ANIDIS L'Ingegneria Sismica in Italia ANIDIS, BOLOGNA. Jun. 2009.
[72] Abruzzo Regione. Modello digitale del terreno - risoluzione 10x10 metri [Online]. Available: http://opendata.regione.abruzzo.it/content/modello-digitale-del-terreno-risoluzione-10x10-metri.
[73] MIT. *Norme tecniche per le costruzioni (NTC 2018)*, Roma. Feb. 20, 2018.
[74] Magenes G, Penna A, Galasco A, Rota M. Experimental characterisation of stone masonry mechanical properties. Presented at the 8th international masonry conference. Dresden; 2010.
[75] Senaldi I, et al. Natural stone masonry characterization for the shaking-table test of a scaled building specimen. Presented at the 10th international masonry conference. 2018. Milan.
[76] Ministero delle Infrastrutture e dei Trasportidelle Infrastrutture. Norme Tecniche per le Costruzioni (NTC 2008). 2008.
[77] Kohrangi M, Bazzurro P, Vamvatsikos D, Spillatura A. Conditional spectrum-based ground motion record selection using average spectral acceleration. Earthq Eng Struct Dynam 2017;46(10). https://doi.org/10.1002/eqe.2876. Art. no. 10.
[78] Ozsarac Volkan, Monteiro Ricardo, Calvi Gian Michele. Probabilistic seismic assessment of reinforced concrete bridges using simulated records. Structure and Infrastructure Engineering 2021;19(4):554–74. https://doi.org/10.1080/15732479.2021.1956551. https://www.tandfonline.com/doi/full/10.1080/15732479.2021.1956551. [Accessed 22 July 2021].
[79] Pagani M, Monelli D, Weatherill G, Danciu L, Crowley H, Silva V, Henshaw P, Butler L, Nastasi M, Panzeri L, Simionato M, Vigano D. OpenQuake Engine: An Open Hazard (and Risk) Software for the Global Earthquake Model. Seismological Research Letters 2014;85(3):692–702. https://doi.org/10.1785/0220130087. https://pubs.geoscienceworld.org/srl/article/85/3/692-702/315386. [Accessed 3 May 2014].
[80] Danciu Laurentiu, Giardini Domenico, Weatherill Graeme, Basili Roberto, Nandan Shyam, Rovida Andrea, Beauval Céline, Bard Pierre-Yves, Pagani Marco, Reyes Celso G, Sesetyan Karin, Vilanova Susana, Cotton Fabrice, Wiemer Stefan. The 2020 European Seismic Hazard Model: overview and results. Natural Hazards and Earth System Sciences 2024;24(9):3049–73. https://doi.org/10.5194/nhess-24-3049-2024. https://nhess.copernicus.org/articles/24/3049/2024/. [Accessed 13 September 2024].
[81] Kottke AR, Rathje EM. Technical manual for strata, 2008/10. Berkeley: Pacific Earthquake Engineering Research Center, University of California; 2008.
[82] Gazetas G. Formulas and charts for impedances of surface and embedded foundations. J Geotech Eng Sep. 1991;117(9):1363–81. https://doi.org/10.1061/(ASCE)0733-9410(1991)117:9(1363).

[83] Pais A, Kausel E. Approximate formulas for dynamic stiffnesses of rigid foundations. Soil Dynam Earthq Eng Oct. 1988;7(4):213–27. https://doi.org/10.1016/S0267-7261(88)80005-8.

[84] de Silva F, Silvestri F. Derivation, validation, and web application of dimensionless analytical solutions for equivalent period and damping ratio of soil-foundation-structure systems. J Geotech Geoenviron Eng Jun. 2025;151(6):04025049. https://doi.org/10.1061/JGGEFK.GTENG-12927.

[85] Givens MJ, Mylonakis G, Stewart JP. Modular analytical solutions for foundation damping in soil-structure interaction applications. Earthq Spectra Aug. 2016;32(3):1749–68. https://doi.org/10.1193/071115EQS112M.

[86] EN 1997-1. "Eurocode 7: geotechnical design - part 1: general rules," authority: the European Union per regulation 305/2011, directive 98/34/EC, directive 2004/18/EC. 2004 [Online]. Available: https://eurocodes.jrc.ec.europa.eu/EN-Eurocodes/eurocode-7-geotechnical-design. [Accessed 22 August 2024].